

Galaxy density profiles and shapes – I. simulation pipeline for lensing by realistic galaxy models

Glenn van de Ven^{1*}, Rachel Mandelbaum^{1†}, Charles R. Keeton^{2‡}

¹*Institute for Advanced Study, Einstein Drive, Princeton NJ 08540, USA*

²*Department of Physics and Astronomy, Rutgers University, 136 Frelinghuysen Road, Piscataway NJ, 08854, USA*

29 August 2021

ABSTRACT

Studies of strong gravitational lensing in current and upcoming wide and deep photometric surveys, and of stellar kinematics from (integral-field) spectroscopy at increasing redshifts, promise to provide valuable constraints on galaxy density profiles and shapes. However, both methods are affected by various selection and modelling biases, which we aim to investigate in a consistent way. In this first paper in a series we develop a flexible but efficient pipeline to simulate lensing by realistic galaxy models. These galaxy models have separate stellar and dark matter components, each with a range of density profiles and shapes representative of early-type, central galaxies without significant contributions from other nearby galaxies. We use Fourier methods to calculate the lensing properties of galaxies with arbitrary surface density distributions, and Monte Carlo methods to compute lensing statistics such as point-source lensing cross-sections. Incorporating a variety of magnification bias modes lets us examine different survey limitations in image resolution and flux. We rigorously test the numerical methods for systematic errors and sensitivity to basic assumptions. We also determine the minimum number of viewing angles that must be sampled in order to recover accurate orientation-averaged lensing quantities. We find that for a range of non-isothermal stellar and dark matter density profiles typical of elliptical galaxies, the combined density profile and corresponding lensing properties are surprisingly close to isothermal around the Einstein radius. The converse implication is that constraints from strong lensing and/or stellar kinematics, which are indeed consistent with isothermal models near the Einstein radius, cannot trivially be extrapolated to smaller and larger radii.

Key words: gravitational lensing – stellar dynamics – galaxies: photometry – galaxies: kinematics and dynamics – galaxies: structure – methods: numerical

1 MOTIVATION

1.1 Learning from galaxy density profiles and shapes

Observational constraints on galaxy density profiles and shapes can be used to study a great variety of problems, from basic cosmology to the connections between dark matter and baryons. For example, the spherically-averaged form of the dark matter halo density profile, and the distribution of halo shapes, both depend on cosmological parameters to the extent that those parameters affect the process of structure formation (e.g., Bullock et al. 2001;

Allgood et al. 2006), and on the physics of galaxy formation to the extent that baryons modify the dark matter distribution (e.g., Blumenthal et al. 1986; Gnedin et al. 2004; Kazantzidis et al. 2004; Naab et al. 2007; Rudd et al. 2008). While there is still some disagreement in the literature about the theoretical predictions, even among those papers cited above, one key result is that there is considerable scatter in both the density profiles and shapes of dark matter halos, which presumably reflects different formation histories (e.g., Wechsler et al. 2002).

Several observational tools have been used to constrain the density profiles and shapes of galaxies, at different length and mass scales, and redshifts. The main tools we consider are gravitational lensing and stellar kinematics. X-ray data are also useful for understanding the density profiles and shapes of massive galaxies and galaxy clusters, but are beyond the scope of our investigation.

* glenn@ias.edu, Hubble Fellow

† rmandelb@ias.edu, Hubble Fellow

‡ keeton@physics.rutgers.edu

Gravitational lensing is the deflection of light from distant sources by the gravitational fields of intervening lens galaxies. Strong lensing occurs in the central regions of galaxies (and clusters) where the light bending is extreme enough to produce multiple images of a background source. It can be used to study the mass distributions of individual galaxies on projected scales of typically several kpc (for a review, see Kochanek 2006). Weak lensing is a complementary phenomenon in which the deflection of light slightly distorts the shapes of background sources without creating multiple images (for a review, see Bartelmann & Schneider 2001). Weak lensing probes galaxy mass distributions on scales from tens of kpc out to about 10 Mpc, but only yields constraints on ensemble averages, since currently weak lensing by galaxies can only be detected by stacking many lens galaxies. While galaxy clusters can be studied on an individual basis using weak lensing, our focus is on galaxies.

High-quality (two-dimensional) data on the kinematics of stars as well as gas in the inner parts (a few to ten kpc) of galaxies are now readily available, thanks in particular to strong progress in integral-field spectroscopy in the last decade. Kinematics in the outer parts of late-type galaxies can often be observed from the presence of neutral hydrogen (e.g., Bosma 1981; van Albada et al. 1985; Persic et al. 1996; Noordermeer et al. 2007). In the outer parts of early-type galaxies, however, cold gas is scarce (but see e.g. Franx et al. 1994; Morganti et al. 1997; Weijmans et al. 2008), so we are left with discrete kinematic tracers such as planetary nebulae and globular cluster (e.g., Côté et al. 2003; Douglas & et al. 2007) out to tens of kpc.

Current and upcoming wide and deep photometric surveys will reveal a vast number of strong lensing events (e.g., Fassnacht et al. 2004; Koopmans et al. 2004; Kuhlen et al. 2004; Marshall et al. 2005), and will also allow for extensive, complementary weak lensing analysis (e.g. Tyson 2002; Kaiser 2004). At the same time, there is a rapid increase in the availability of two-dimensional kinematics of galaxies nearby (e.g., Emsellem & et al. 2004; McDermid & et al. 2006), and even at high(er) redshift (e.g., van der Marel & van Dokkum 2007; Bouché & et al. 2007). These data sets, individually as well as combined, may provide strong constraints on galaxy density profiles and shapes, but the analyses involved are subject to selection and modelling biases.

1.2 Selection and modelling biases

If we want to use strong lensing and kinematics to make robust tests of cosmological predictions, we need to answer two questions: Can strong lensing and kinematic analyses yield accurate constraints on galaxy density profiles? Are the galaxies in which we can make the measurements (especially in the case of strong lensing) representative of all galaxies? We refer to these two concerns as *modelling biases* and *selection biases*, respectively.

The question of selection bias is particularly important given the diversity in the galaxy population. It is well known that strong lensing favours early-type over late-type galaxies, and massive galaxies over dwarfs (e.g., Turner et al. 1984; Fukugita & Turner 1991). But even within the population of massive early-type galaxies, to what extent does strong lensing favour galaxies whose dark matter halos have

inner slopes that are steeper than average, or concentrations that are higher than average? Also, to what extent does strong lensing favour galaxies with particular shapes and/or orientations with respect to the line-of-sight? To phrase these questions formally, consider some parameter x describing the galaxy density profile or shape (e.g., the inner slope of the dark matter density profile). We need to understand how the distribution $p_{\text{SL}}(x)$ among strong lens galaxies compares to the underlying distribution $p(x)$ for all galaxies. Any analysis that includes strong lensing with some other technique used to study the same systems will suffer from strong lensing-related selection biases, since we never get to choose which systems will be a strong lens. Selection biases are critical when we want to interpret constraints on lens galaxy density profiles and/or shapes from strong lensing, possibly in combination with kinematics (e.g. Rusin & Kochanek 2005; Koopmans et al. 2006) in comparison with predictions from cosmological models.

On the other hand, modelling biases may occur because of (often unavoidable) assumptions made when analysing gravitational lensing and/or kinematic data because of the finite number of constraints available from the data. Since galaxies are in general non-spherical, we can only correctly interpret the observations if we know the viewing direction, and even then the deprojection might not be unique (e.g. Rybicki 1987). Moreover, strong lensing is subject to the so-called mass-sheet degeneracy: part of the deflection and magnification of the light from the background source can be due to mass along the line-of-sight that is not associated with the lens galaxy itself¹. In addition, the constraints from strong lensing on the galaxy density are typically limited in radius to around the Einstein radius, and even then, without secure, unaffected measurements of the flux of the lensing images, the density profile is difficult to recover. Kinematics can be obtained over a larger radial extent, but in particular stellar kinematics suffer from the so-called mass-anisotropy degeneracy: a change in the measured line-of-sight velocity dispersion can be due to a change in total mass, but may also be the result of velocity anisotropy.

In a series of papers, we are developing a pipeline for using realistic galaxy models to simulate strong lensing and kinematic data, and assess how both selection and modelling biases affect typical strong lensing and kinematic analyses. In this first paper, we present the simulation pipeline for point-source lensing. We focus on strong lensing of quasars by early-type, central galaxies at different mass scales, using two-component mass profiles (dark matter plus stellar component) that are consistent with existing photometry and stacked weak lensing data from SDSS (Kauffmann & et al. 2003; Mandelbaum et al. 2006b), N -body, and hydrodynamic simulations. In Mandelbaum et al. (2008, hereafter Paper II), we use this pipeline to study selection biases in strong lensing surveys. In future work we will address modelling biases in strong lensing and kinematics (both when studied separately and when combined). Our overall goal is to determine how strong lensing, kinematics, and possibly other probes (weak lensing, and X-ray data for cluster mass

¹ Part of this mass-sheet degeneracy may be overcome in future surveys through the measurements of time delays for an adopted Hubble constant.

scales) can be used to obtain robust, unbiased constraints on galaxy density profiles and shapes.

To make our presentation coherent, and to clarify our notation and terminology, we first review the analytic treatment of ellipsoidal mass distributions with different profiles and shapes (Section 2), and the basic theory of strong lensing (Section 3). We then describe our simulation pipeline for point-source lensing in depth. In Section 4 we present our choices for the masses, profiles, and shapes of the galaxy models. In Section 5 we discuss the numerical methods we use for lensing calculations, including numerous tests. A summary of the simulation pipeline, and some implications for strong lensing analyses are given in Section 6.

2 GALAXY DENSITY PROFILES AND SHAPES

In this section we describe our treatment of galaxy density profiles and shapes. While our approach is fairly conventional, it is important to present it carefully to clarify our notation and terminology, collect useful technical results, and provide a firm foundation for the work in this series of papers. This section focuses on the formal framework; the specific galaxy models used in our simulations are discussed in Section 4.

2.1 Notation

We compute distances using a flat Λ CDM cosmology with $\Omega_m = 0.27$ and $h = 0.72$. We use x , y , and z to denote intrinsic, three-dimensional (3d) coordinates, and x' and y' for the projected, two-dimensional (2d) coordinates. Similarly, r is the intrinsic radius ($r^2 = x^2 + y^2 + z^2$) and R' is the projected radius ($R'^2 = x'^2 + y'^2$). For non-spherical galaxies, we use a , b , and c for the major, intermediate, and minor semi-axis lengths of the intrinsic, 3d density profiles; and we use a' and b' for the major and minor semi-axis lengths of the projected, 2d surface densities. Subscripts “dm” and “ \star ” are used to indicate whether a quantity describes the dark matter or stellar component of the galaxy model. Any gas component that has not cooled to form stars — which is expected to be subdominant relative to the stellar component for early type galaxies (e.g. Read & Trentham 2005; Morganti & et al. 2006) — is implicitly included in the component that we label dark matter.

2.2 Ellipsoidal shapes

We consider mass density distributions $\rho(x, y, z) = \rho(m)$ that are constant on ellipsoids

$$m^2 = \frac{x^2}{a^2} + \frac{y^2}{b^2} + \frac{z^2}{c^2}, \quad (1)$$

with $a \geq b \geq c$. The major semi-axis length a is a scale parameter, whereas the intermediate-over-major (b/a) and minor-over-major (c/a) axis ratios determine the shape. In the oblate or prolate axisymmetric limit we have $a = b > c$ (pancake-shaped) or $a > b = c$ (cigar-shaped), respectively, while in the spherical limit $a = b = c$ (so then $m = r/a$). Note that m is a dimensionless ellipsoidal radius.

Under the thin-lens approximation, the gravitational

lensing properties are fully characterised by the mass density projected along the line-of-sight. We introduce a new Cartesian coordinate system (x'', y'', z'') , with x'' and y'' in the plane of the sky and the z'' -axis along the line-of-sight. Choosing the x'' -axis in the (x, y) -plane of the intrinsic coordinate system (cf. de Zeeuw & Franx 1989 and their Fig. 2), the transformation between both coordinate systems is known once two viewing angles, the polar angle ϑ and azimuthal angle φ , are specified. The intrinsic z -axis projects onto the y'' -axis; for an axisymmetric galaxy model the y'' -axis aligns with the short axis of the projected mass density,² but for a triaxial galaxy model the y'' -axis is misaligned by an angle $\psi \in [-\pi/2, \pi/2]$ such that (cf. equation B9 of Franx 1988)

$$\tan 2\psi = \frac{T \sin 2\varphi \cos \vartheta}{\sin^2 \vartheta + T (\sin^2 \varphi \cos^2 \vartheta - \cos^2 \varphi)}, \quad (2)$$

where T is the triaxiality parameter defined as $T = (a^2 - b^2)/(a^2 - c^2)$. A rotation through ψ transforms the coordinate system (x'', y'', z'') to (x', y', z') such that the x' and y' axes are aligned with the major and minor axes of the projected mass density (respectively), while $z' = z''$ is along the line-of-sight (see also Section 4.4.3 below).

Projecting $\rho(m)$ along the line-of-sight yields a surface mass density $\Sigma(x', y') = \Sigma(m')$ that is constant on ellipses in the sky-plane,

$$\Sigma(m') = \int_{-\infty}^{\infty} \rho(m) dz' = \frac{abc}{a'b'} 2 \int_0^{\infty} \rho(m) m du, \quad (3)$$

where we have used $z' = abc \sinh(u)/(a'b') + \text{constant}$, and $m = m' \cosh(u)$. The sky-plane ellipse is given by

$$m'^2 = \frac{x'^2}{a'^2} + \frac{y'^2}{b'^2}. \quad (4)$$

The projected major and minor semi-axis lengths, a' and b' , depend on the intrinsic semi-axis lengths a , b , and c and the viewing angles ϑ and φ as follows:

$$a'^2 = \frac{2A^2}{B - \sqrt{B^2 - 4A^2}}, \quad b'^2 = \frac{2A^2}{B + \sqrt{B^2 - 4A^2}}, \quad (5)$$

where A and B are defined as

$$A^2 = a^2 b^2 \cos^2 \vartheta + (a^2 \sin^2 \varphi + b^2 \cos^2 \varphi) c^2 \sin^2 \vartheta, \quad (6)$$

$$B = a^2 (\cos^2 \varphi \cos^2 \vartheta + \sin^2 \varphi) + b^2 (\sin^2 \varphi \cos^2 \vartheta + \cos^2 \varphi) + c^2 \sin^2 \vartheta. \quad (7)$$

It follows that $A = a'b'$ is proportional to the area of the ellipse.

The flattening b'/a' of the projected ellipses actually depends on the viewing angles (ϑ, φ) and the intrinsic axis ratios $(b/a, c/a)$, and is independent of the scale length. Since the intrinsic and projected semi-major axis lengths are directly related via the left equation of (5), the scale length can be set by choosing either a or a' .

Finally, we define the negative logarithmic slope of the mass density $\gamma(m) = -d \ln \rho(m)/d \ln m$ and of the surface

² For an oblate galaxy, the alignment ($\psi = 0$) follows directly from equation (2) since $T = 0$. For a prolate galaxy it is most easily seen by exchanging a and c ($c > b = a$), so that the z -axis is again the symmetry axis (instead of the x -axis).

mass density $\gamma'(m') = -d \ln \Sigma(m')/d \ln m'$. Substituting equation (3), the latter follows as

$$\gamma'(m') = \frac{\int_0^\infty [\gamma(m) - 1] \rho(m) m' du}{\int_0^\infty \rho(m) m du}, \quad (8)$$

which in general has to be evaluated numerically.

2.3 Choice of density profiles

We consider two families of density profiles, motivated by both observations and simulations of galaxies. Historically, there has been considerable interest in cusped density profiles that have a shallower power-law at small radii and a steeper power-law at large radii, with a smooth transition in between. This family includes the Hernquist (1990) profile that is commonly used to model the stellar components of early-type galaxies and spiral galaxy bulges, along with (generalised) NFW (Navarro et al. 1997) profiles often used to describe the dark matter profiles of simulated galaxies.

An alternative, observationally motivated family of models is obtained by deprojecting the Sérsic (1968) profile that is known to give a good fit to the surface brightness profiles of early-type galaxies and spiral galaxy bulges. There have been claims that deprojected Sérsic profiles actually provide a better fit to simulated dark matter halos than (generalised) NFW profiles (e.g., Navarro & et al. 2004; Merritt et al. 2005). Several recent studies argue that a Sérsic profile that is not deprojected —also referred to as an Einasto (1965) profile— provides an even better fit (Merritt et al. 2006; Gao L. and Navarro), although when compared against a generalised NFW or Sérsic profile the improvement is marginal at best.

X-ray (e.g., Allen et al. 2001, 2002; Vikhlinin et al. 2005, 2006) and weak lensing (e.g., Kneib et al. 2003; Limousin et al. 2007) observations of individual galaxy clusters suggest that outside of ~ 50 kpc, the density profiles are consistent with the NFW profiles seen in N-body simulations (no attempts were made to compare with the Sérsic model, however). The mass range for these observations is about a factor two above our higher mass model.

Since there is still no consensus opinion about which models are best, we consider how the choice of density profile affects our conclusions by using both cusped density profiles and deprojected Sérsic density profiles

2.4 Cusped density profiles

The cusped density distribution with inner slope γ and outer slope n ,

$$\rho(m) = \frac{\rho_0}{m^\gamma (1+m)^{n-\gamma}}, \quad (9)$$

includes the following well-known spherical ($m = r/a$) density profiles: $(\gamma, n) = (1, 4)$, the Hernquist profile (Hernquist 1990); $(2, 4)$, the Jaffe profile (Jaffe 1983); and $(1, 3)$, the NFW profile (Navarro et al. 1997).

The mass enclosed within the ellipsoidal radius m (for inner slopes $\gamma < 3$) is

$$M(m) = 4\pi abc\rho_0 \left(\frac{m}{1+m}\right)^{3-\gamma} \frac{1}{3-\gamma} \times {}_2F_1\left[n-\gamma, 3-\gamma; 4-\gamma; \frac{m}{1+m}\right], \quad (10)$$

where ${}_2F_1[\alpha, \beta, \gamma; x]$ is the hypergeometric function. For outer slopes $n > 3$, equation (10) reduces to $M(m) = 4\pi abc\rho_0 \beta[n-3, 3-\gamma; m/(1+m)]$. When $m \rightarrow \infty$, the latter incomplete beta function becomes the complete beta function $\beta[n-3, 3-\gamma]$, and we obtain a finite total mass.

Substituting $n = 4$ into equation 10 yields $M(m) = 4\pi abc\rho_0 [m/(1+m)]^{3-\gamma}/(3-\gamma)$, so that for $\gamma = 1$, we find the total mass $M = 2\pi abc\rho_0$ of the Hernquist profile, which we adopt for the stellar component when using cusped density profiles. For outer slopes $n \leq 3$, the total mass is infinite, but for certain half-integer values of γ and n the expression for the enclosed mass simplifies significantly. For example, for $n = 3$, the value which we adopt for the outer slope of the dark matter profile, we find

$$\frac{M(m)}{4\pi abc\rho_0} = \begin{cases} \ln(1+m) - m(2+3m)/[2(1+m)^2], \\ 2\sinh^{-1}(\sqrt{m}) - 2\sqrt{m}(4m+3)/[3(1+m)^{3/2}], \\ \ln(1+m) - m/(1+m), \\ 2\sinh^{-1}(\sqrt{m}) - 2\sqrt{m}/(1+m), \\ \ln(1+m), \end{cases} \quad (11)$$

for inner slope values of $\gamma = \{0, 1/2, 1, 3/2, 2\}$, respectively.

Although for certain values of γ and n , lengthy analytic expressions for the surface mass density $\Sigma(m')$ can be derived, we evaluate the integral in equation (3) numerically. The logarithmic slope $\gamma(m)$ of the cusped density profile is

$$\gamma(m) = (\gamma + mn)/(1+m), \quad (12)$$

while $\gamma'(m')$ of the surface mass density follows from numerical evaluation of equation (8).

2.5 Deprojected Sérsic density profiles

It has long been known that the surface brightness profiles of early-type galaxies and of spiral galaxy bulges are well fit by a Sérsic (1968) profile $I(R) \propto \exp[-(R/R_e)^{1/n}]$, with the effective radius R_e enclosing half of the total light. A key conceptual difference from the cusped models is that the profile does not converge to a particular inner slope on small scales. The deprojection of the Sérsic profile has to be done numerically. However, the analytic density profile of Prugniel & Simien (1997),

$$\rho(m) = \frac{\rho_0}{m^{p_n}} \exp[-b_n m^{1/n}], \quad (13)$$

provides a good match to the deprojected Sérsic profile when the inner negative slope is given by

$$p_n = 1 - \frac{0.6097}{n} + \frac{0.05563}{n^2}. \quad (14)$$

The enclosed mass for the Prugniel-Simien model is

$$M(m) = 4\pi abc\rho_0 n b_n^{(p_n-3)n} \gamma[(3-p_n)n, b_n m^{1/n}], \quad (15)$$

where $\gamma[p; x]$ is the incomplete gamma function, which in the case of the total mass reduces to the complete gamma function $\Gamma[p] = \gamma[p; \infty]$.

The expression for the surface mass density is, to high accuracy, the Sérsic profile

$$\Sigma(m') = \Sigma_0 \exp[-b_n (m')^{1/n}]. \quad (16)$$

Given the enclosed projected mass

$$M'(m') = 2\pi a' b' \Sigma_0 n b_n^{-2n} \gamma[2n, b_n (m')^{1/n}], \quad (17)$$

the requirement that the total intrinsic and projected mass have to be equal yields a normalisation

$$\Sigma_0 = \frac{abc}{a'b'} \rho_0 \frac{2\Gamma[(3-p_n)n]}{b_n^{(1-p_n)n} \Gamma[2n]}. \quad (18)$$

The value of b_n depends on the index n and the choice for the scale length. The latter is commonly chosen to be the effective radius R_e in the surface brightness profile, which contains half of the total light. We adopt a similar convention requiring that the ellipse $m' = 1$ contains half of the projected mass. This choice results in the relation $\Gamma[2n] = 2\gamma[2n, b_n]$, which to high precision can be approximated by (Ciotti & Bertin 1999)

$$b_n = 2n - \frac{1}{3} + \frac{4}{405} \frac{1}{n} + \frac{46}{25515} \frac{1}{n^2}. \quad (19)$$

The logarithmic slope of the Prugniel-Simien and Sérsic profile are related by

$$\gamma(m) = p_n + \gamma'(m), \quad (20)$$

where the logarithmic slope of the surface mass density is

$$\gamma'(m') = (b_n/n) (m')^{1/n}. \quad (21)$$

3 STRONG LENSING

In this section, we review the strong lensing concepts that are most important for our work. See Schneider et al. (1992) and Kochanek (2006) for more discussion of strong lensing theory. The specific lensing calculations used in our simulations are discussed in Section 5.

3.1 Basic theory

The gravitational lensing properties of a galaxy with surface mass density $\Sigma(R')$ are characterised by the lens potential ϕ (in units of length squared) that satisfies the two-dimensional Poisson equation

$$\nabla^2 \phi = 2\kappa, \quad \text{where } \kappa \equiv \Sigma/\Sigma_c. \quad (22)$$

Here κ is the surface mass density scaled by the critical density for lensing (Σ_c , see Section 3.2), and is referred to as the ‘‘convergence.’’ The positions and magnifications of lensed images depend on the first and second derivatives of the lens potential, respectively. The image positions are the solutions of the lens equation,

$$\vec{\beta} = \vec{\theta} - \vec{\alpha}(\vec{\theta}), \quad (23)$$

where $\vec{\alpha} = \vec{\nabla}\phi$ is the deflection angle (in units of length), while $\vec{\theta} = (\theta_1, \theta_2)$ and $\vec{\beta} = (\beta_1, \beta_2)$ are two-dimensional angular positions on the sky in the lens and source planes, respectively. The angular coordinates are related to the projected physical coordinates by $\theta_1 = x'/D_L$ and $\theta_2 = y'/D_L$, where D_L is the angular diameter distance to the lens; and

$\beta_1 = x'/D_S$ and $\beta_2 = y'/D_S$, where D_S is the angular diameter distance to the source.³ The magnification of an image at position (x', y') is given by

$$\mu = \left[\left(1 - \frac{\partial^2 \phi}{\partial x'^2} \right) \left(1 - \frac{\partial^2 \phi}{\partial y'^2} \right) - \left(\frac{\partial^2 \phi}{\partial x' \partial y'} \right)^2 \right]^{-1}. \quad (24)$$

A typical lens galaxy has two ‘‘critical curves’’ along which the magnification is formally infinite, which map to ‘‘caustics’’ in the source plane. The caustics bound regions with different numbers of images (see Section 5.7 for examples).

If the lens is circularly symmetric, the deflection is radial and has amplitude

$$\alpha(R') = \frac{2}{R'} \int_0^{R'} \kappa(\tilde{R}') \tilde{R}' d\tilde{R}'. \quad (25)$$

The outer or ‘‘tangential’’ critical curve corresponds to the ring image that would be produced by a source at the origin. The radius of this ring is the Einstein radius R_{ein} , which is given mathematically by the solution of the equation $\alpha(R_{\text{ein}}) = R_{\text{ein}}$. This definition is equivalent to saying that the Einstein radius bounds the region within which the average convergence is unity, such that the enclosed mass $M_{\text{ein}} = \pi R_{\text{ein}}^2 \Sigma_c$. By contrast, the inner or ‘‘radial’’ critical curve has radius R_{rad} given by the solution of $d\alpha/dR' = 1$.

If the lens is non-circular, the conditions for the critical curves and caustics are more complicated, but we can still retain some concepts from the circular case. In particular, we can say that the outer/tangential critical curve is principally determined by the enclosed mass, whereas the inner/radial critical curve is determined by the slope of the deflection curve. When we map the critical curves in the lens plane to the caustics in the source plane, the arrangement of curves is inverted: the outer critical curve corresponds to the inner caustic; while the inner critical curve corresponds to the outer caustic.⁴ Since the outer caustic bounds the multiply-imaged region, it determines the total lensing cross-section. This means the cross-section is sensitive to the surface mass density (in particular its logarithmic slope) at small radii in the lens plane, which will be important to bear in mind when interpreting our results.

While a non-circular lens has non-circular critical curves, it is still occasionally useful to characterise the scale for strong lensing with a single Einstein radius. We generalise the definition of the Einstein radius to a non-circular lens by using the monopole deflection, or the deflection angle produced by the monopole moment of the lens galaxy,

$$\alpha_0(R') = \frac{1}{\pi R'} \int_0^{2\pi} \int_0^{R'} \kappa(\tilde{R}, \tilde{\theta}) \tilde{R} d\tilde{R} d\tilde{\theta} = R' \bar{\kappa}(R'), \quad (26)$$

where $\bar{\kappa}(R')$ is the average convergence within radius R' ,

³ Note that because of this trivial conversion between angular and physical units, we do not explicitly distinguish between angles and lengths in the lens plane. For example in the text we refer to the deflection angle in physical units (e.g., by stating that $\alpha(R_{\text{ein}}) = R_{\text{ein}}$) whereas our plots may show α in angular units.

⁴ If the lens is highly flattened, the tangential caustic can actually pierce the radial caustic; some specific examples are discussed below (e.g., Section 5.7). However, this situation is unusual, and it does not substantially alter the present discussion.

and $(\tilde{R}, \tilde{\theta})$ are polar coordinates on the sky. The Einstein radius is then given by $\alpha_0(R_{\text{ein}}) = R_{\text{ein}}$, or equivalently $\bar{\kappa}(R_{\text{ein}}) = 1$. This is the definition that emerges naturally from models of non-spherical lenses (e.g., Cohn et al. 2001), and it matches the conventional definition in the circular case.

It is instructive to think of lensing in terms of Fermat’s principle and say that lensed images form at stationary points of the arrival time surface (e.g., Blandford & Narayan 1986). Since the arrival time is a 2d function of angles on the sky, there are three types of stationary points: minima, maxima, and saddle points. We can classify them using the eigenvalues of the inverse magnification tensor,

$$\lambda_{\pm} = (1 - \kappa) \pm \gamma, \quad \text{where} \quad \gamma = [(1 - \kappa)^2 - \mu^{-1}]^{1/2}. \quad (27)$$

Here, γ is the shear⁵, which quantifies how much a resolved image is distorted. The eigenvalues are both positive for a minimum, both negative for a maximum, and mixed for a saddle point. Since our galaxies have central surface densities shallower than $\Sigma \propto R'^{-1}$, the lensing “odd image theorem” applies: the total number of images must be odd, and the number of minimum, maximum, and saddle point images must satisfy the following relation (Burke 1981; Schneider et al. 1992):

$$N_{\text{min}} + N_{\text{max}} = N_{\text{sad}} + 1. \quad (28)$$

In practice, images at maxima are rarely observed because they form near the centres of lens galaxies and are highly demagnified; the only secure observation of a maximum image in a galaxy-scale lens required a deep and dedicated search (Winn et al. 2004). We do compute maxima because they are useful in checking our numerical methods (see Section 5.2), but we focus our analysis on minimum and saddle point images because they constitute the bulk of lensing astrophysics.

3.2 Redshift dependence

The redshifts of the lens (z_L) and source (z_S) play an important role in determining what region of a galaxy is relevant for strong lensing. Roughly speaking, strong lensing occurs in the region where the surface mass density exceeds the critical density for lensing,

$$\Sigma_c = \frac{c^2}{4\pi G} \frac{D_S}{D_L D_{LS}}, \quad (29)$$

where the D values are the angular diameter distances to the lens (D_L), to the source (D_S), and from the lens to the source (D_{LS}). Note that D_{LS} can be computed for a flat universe using the relation

$$D_{LS} = D_S - \left(\frac{1 + z_L}{1 + z_S} \right) D_L, \quad (30)$$

and for more general cosmologies, see Hogg (1999). For a fixed source redshift, Σ_c is lowest when the lens is roughly

⁵ In general the shear has two components conveniently expressed in complex notation (e.g. Schneider et al. 1992), but as usual in strong lensing analyses we only use the amplitude (or norm) for which γ is the standard symbol. The context should make clear whether we are using γ to refer to a lensing shear or to the negative logarithmic slope of the density profile.

halfway between the observer and source, and it increases as the lens moves toward the observer or source. For a fixed lens redshift, the critical density is formally infinite for $z_S \leq z_L$, and it decreases monotonically as the source redshift increases past z_L .

We adopt fiducial redshifts of $z_L = 0.3$ for the lens and $z_S = 2$ for the source. The resulting critical density, $\Sigma_c = 2389 M_{\odot} \text{pc}^{-2}$, is such that quasar images generally appear at about one effective radius from the centre of the lens galaxies. At this radius, the stellar component and dark matter halo may both play significant roles in the lensing signal, which is important to keep in mind when interpreting our results in this and subsequent papers.

Our results apply equally well to any other combination of lens and source redshifts that yield $\Sigma_c = 2389 M_{\odot} \text{pc}^{-2}$. The reason is that if we fix the galaxy density profile and vary z_L and z_S so as to keep Σ_c fixed, the strong lensing region will always have the same physical scale and hence the same relation to the density profile. If we instead vary z_L and z_S in a way that increases Σ_c , that will tend to push the lensed images to smaller radii and hence make the stellar component somewhat more dominant. Conversely, varying the redshifts in a way that lowers Σ_c will tend to make the dark matter component more significant. We examine the effect of varying z_L and z_S on our results explicitly in subsequent papers.

We note that the lens redshift also affects strong lensing in the conversion from physical to angular scales. Even if the physical size of the lensing region stays fixed as we vary the source and lens redshifts, the angular separation between the lensed images will vary with z_L . This may lead to *observational* selection effects: for example, resolution-limited surveys may miss lenses for which z_L is high and the images cannot be resolved, while spectroscopic surveys may miss lenses for which z_L is low and the images fall outside the spectroscopic slit or fiber. However, our focus in this work is on *physical* selection biases in strong lensing, which means that we consider the lens and source redshifts only in terms of how they affect Σ_c .

Our choice $z_S = 2$ for the source redshift is typical of quasar lenses in the CASTLES⁶ sample, but our choice $z_L = 0.3$ places the lens galaxy on average at a smaller distance. The latter is, however, closer to the typical lens redshift in the SLACS sample of galaxy/galaxy strong lenses (Bolton et al. 2006, 2008a), but those lenses are explicitly selected to have source redshifts $z_S \lesssim 0.8$ (Bolton et al. 2004). As a result, our fiducial value of Σ_c is typically between that of CASTLES and SLACS lenses. The Einstein radii at $\sim 1 R_e$ in our case appear at larger radii in the CASTLES sample ($2 - 3 R_e$; Rusin & et al. 2003), and at smaller radii in the SLACS sample ($0.3 - 0.9 R_e$; Koopmans et al. 2006). The statistics of the SLACS survey are much more involved than the statistics of quasar lens surveys, because SLACS lenses have extended rather than point-like sources, and the survey relies on fiber spectra from SDSS. SLACS lens statistics have recently been examined by Dobler et al.

⁶ CASTLES (see <http://cfa-www.harvard.edu/castles/>) is a collection of uniform HST observations of mostly point-source lenses from several samples with differing selection criteria, rather than a single, uniformly-selected survey.

(2008), and we do not consider them explicitly in the current work.

4 CONSTRUCTION OF GALAXY MODELS

In this section we construct the galaxy models used in our simulations. We seek models with a variety of density profiles and shapes that not only are realistic but also sample the range of systematic effects in strong lensing. To that end, we must carefully consider the mass and length scales (Sections 4.1–4.2), the profiles (Section 4.3), and the shapes (Section 4.4) of both the stellar and dark matter components. In addition to a main set of simulations with cusped density profiles, we also create a subset of simulations based on deprojected Sérsic density profiles (Section 4.5). After discussing the choice of the model parameters, we briefly describe the part of our pipeline that computes surface mass density maps for these models (Section 4.6), which can then be used for lensing calculations (Section 5).

4.1 Mass scales

We use stellar and dark matter halo masses from SDSS for early-type galaxies, where analyses of the spectra give an estimate of the stellar mass (Kauffmann & et al. 2003), and weak lensing analyses from $0.02\text{--}2h^{-1}\text{ Mpc}$ yield the dark matter mass (Mandelbaum et al. 2006b). The former are subject to systematic uncertainties due to the initial mass function (IMF) at the $\sim 20\text{--}30$ per cent level, whereas the latter is subject to ~ 10 per cent uncertainty in the modelling in addition to $\sim 10\text{--}15$ per cent statistical error.

The selection of mass scales begins with the ansatz that we would like to approximately bracket the typical luminosity and mass range of observed lensing systems. Given the range of lens galaxy luminosities in the CASTLES and SLACS strong lens samples, we choose models with total luminosities of $\sim 2L_*$ and $\sim 7L_*$ in the (SDSS) r -band. We refer to the lower-luminosity model interchangeably as “galaxy scale” or “lower mass scale” model. The higher-luminosity model is essentially a massive galaxy with convergence that is significantly boosted by a group dark matter halo, but we often refer to it as a “group scale” or “higher mass scale” model for brevity. In both cases, the model includes concentric stellar and dark matter components; thus, our current results cannot be applied to satellites in groups/clusters, which will be the subject of future work. We also neglect contributions of nearby (satellite) galaxies to the surface density, focusing only on the host galaxy, and we neglect contributions from other structures along the line of sight (e.g. Keeton & Zabludoff 2004; Momcheva et al. 2006; Williams et al. 2006). The masses are selected from the Mandelbaum et al. (2006b) SDSS weak lensing analysis using results for early-type galaxies as a function of luminosity, as shown in Table 3 or Fig. 4 of that paper.

The model parameters for these mass scales are summarised in Table 1. We define the virial radius entirely using comoving quantities, with r_{180} satisfying the relation

$$180\bar{\rho} = \frac{3M_{180}}{4\pi r_{180}^3}, \quad (31)$$

where M_{180} is the virial mass and $\bar{\rho}$ is the mean density of

the universe (using $\Omega_m = 0.27$). The definition is in principle arbitrary, but this choice was used to analyse the weak lensing results. In the weak lensing results, the profiles were found to be consistent with NFW for early-type galaxies on all scales studied (see also Mandelbaum et al. 2006a, which focuses on $z \sim 0.25$ Luminous Red Galaxies). Thus, not only our use of the masses, but also the form of the density profile, is observationally motivated outside of $\sim 20h^{-1}\text{ kpc}$.

4.2 Length scales

We choose the dark matter halo concentration from the Bullock et al. (2001) result that $c_{\text{dm}} \approx 10(M/M_{\text{nl}})^{-0.13}$, after converting to our mass definition and using inner slope $\gamma_{\text{dm}} = 1$, $z_L = 0.3$, $\sigma_8 = 0.75$ and $\Omega_m = 0.27$. The nonlinear mass M_{nl} is the mass in a sphere within which the rms linear density fluctuation is equal to δ_c , the overdensity threshold for spherical collapse. We obtain $c_{\text{dm}} \simeq 8.4$ for the lower mass scale and $c_{\text{dm}} \simeq 5.6$ for the higher mass scale (see also Table 1). The scale radius of the dark matter component then follows as $r_{s,\text{dm}} = r_{180,\text{dm}}/c_{\text{dm}}$.

We determine the scale length of the stellar components based on SDSS photometry of galaxies of the appropriate luminosity. Fitting de Vaucouleurs profiles, i.e., Sérsic profiles with index $n = 4$, to the growth curve of these elliptical galaxies yields the half-light (or effective) radius R_e . Assuming a constant stellar mass-to-light ratio, R_e is equal to the projected stellar half-mass radius $R'_{h,*}$ as given in Table 1. For a Hernquist cusped density profile with $(\gamma_*, n_*) = (1, 4)$ as we adopt for the stellar component, the scale radius follows as $r_{s,*} = R'_{h,*}/1.8153$.

Given the large scatter in dark matter halo concentration values in simulations (0.15 dex; Bullock et al. 2001), we will also redo a subset of the analysis using concentrations lower and higher than the fiducial values used for the main analysis. This work will allow us to quantify biases associated with halo concentration. Realistically, we expect the changes in the concentration c_{dm} to be somewhat degenerate with changes in the inner slope γ_{dm} , as both change the amount of dark matter in the inner parts, although there may be some differences because changing γ_{dm} affects the inner logarithmic slope while changing c_{dm} does not. In Paper II we quantify the approximate degeneracy between changes in c_{dm} and γ_{dm} for the dark matter component, while keeping the stellar component fixed.

4.3 Density profiles

For our main set of simulations, we use Hernquist and generalised NFW profiles for stellar and dark matter components, respectively (cf. Sections 2.3 and 2.4). While there is some uncertainty over the true dark matter profile in N -body simulations (particularly in the inner regions; see Section 2.5), and the initial dark matter profile may in any case be modified due to the presence of baryons, we use the generalised NFW model because it allows freedom in the form of the cusp. As discussed in more detail below (Section 4.5), we also examine how our results depend on the form of the density profiles by running a set of simulations that use deprojected Sérsic profiles for the intrinsic (3d) densities of both the stellar and dark matter components. Here we focus on the main set of simulations with cusped profiles.

Table 1. Summary of the spherical density profile parameters for galaxy and group scale models. With the exception of $R'_{h,*}$, all numbers given are intrinsic (3d).

Description	Symbol	Galaxy-scale	Group-scale	Unit
Dark matter component				
Virial mass	$M_{180,\text{dm}}$	3.4×10^{12}	6.7×10^{13}	$h^{-1} M_{\odot}$
	$M_{180,\text{dm}}$	4.7×10^{12}	9.3×10^{13}	M_{\odot}
Virial radius	$r_{180,\text{dm}}$	390.7	1055	comoving h^{-1} kpc
	$r_{180,\text{dm}}$	417	1127	physical kpc
	$r_{180,\text{dm}}$	97.1	262	arcsec
Concentration	$c_{\text{dm}} (\gamma_{\text{dm}} = 1)$	8.4	5.6	–
Scale radius	$r_{s,\text{dm}} (\gamma_{\text{dm}} = 1)$	49.7	201	physical kpc
	$r_{s,\text{dm}} (\gamma_{\text{dm}} = 1)$	11.56	46.8	arcsec
Stellar component				
Total mass	$M_{\text{tot},*}$	1.16×10^{11}	5.6×10^{11}	M_{\odot}
Half-mass radius (projected)	$R'_{h,*}$	4.07	11.7	kpc
	$R'_{h,*}$	0.95	2.7	arcsec
Scale radius	$r_{s,*} (\gamma_* = 1)$	2.24	6.4	physical kpc
	$r_{s,*} (\gamma_* = 1)$	0.52	1.5	arcsec

4.3.1 Inner and outer slope

For our main set of simulations with cusped density profiles, we fix the stellar component to have a Hernquist profile, with inner slope $\gamma_* = 1$ and outer slope $n_* = 4$. Based on cosmological N -body simulations, we fix the outer slope of the dark matter simulation to $n_{\text{dm}} = 3$ (e.g., Navarro & et al. 2004).

The inner slope of the dark matter profile is more problematic. While N -body simulations can suggest forms for dark matter halo profiles (e.g., Navarro & et al. 2004), there is some question whether those profiles are affected by the presence of a stellar component, and if so, in what way. One formalism for analysing how a stellar component affects a dark matter profile is called adiabatic contraction (AC: Young 1980; Blumenthal et al. 1986; Gnedin et al. 2004; Sellwood & McGaugh 2005). The physical picture is that as the baryons cool and condense into the centre of the system, they draw some of the dark matter in as well, causing the dark matter halo profile to steepen. Persuasive observational evidence for or against AC in the galaxies we are modelling does not yet exist, though there are claims that the theoretical assumptions behind AC are not valid for these galaxies. Naab et al. (2007) suggest that the opposing effect, growth through dissipationless infall of matter onto the galaxy (which tends to push the dark matter outwards from the centre) may cancel out the steepening due to baryonic cooling. We expect the effects of infalling matter to be even more significant for our higher mass model, which is equivalent to a fairly massive group. Furthermore, hydrodynamic simulations that demonstrate that adiabatic contraction dominates may suffer from over-cooling of the baryonic component, so we cannot use them to determine the extent of the effect either. Thus, we cannot be certain how much the dark matter profiles may be modified due to the different processes involved in galaxy formation.

We consider the range of possibilities in two ways. First, for the main set of simulations with cusped density profiles, we examine three values of the dark matter inner slope:

$\gamma_{\text{dm}} = \{0.5, 1.0, 1.5\}$. As we shall see, this allows for a broad range of lensing properties. Second, for a subset of simulations with $\gamma_{\text{dm}} = 1$ NFW dark matter profiles, we explicitly include the effects of AC, using the formalisms in Blumenthal et al. (1986) and Gnedin et al. (2004).

4.3.2 Normalisation

When the inner slope of the dark matter γ_{dm} is changed, the virial mass M_{180} also changes. To preserve M_{180} we must change either the density amplitude ρ_0 or the scale radius r_s of the dark matter (or both at the same time). Preserving in addition the (reduced) shear at the virial radius r_{180} , would break this “degeneracy” in the normalisation. However, for individual strong lens galaxies, weak lensing and other constraints on the density are very weak if present at all. Nevertheless, the different choices for the normalisation might not result in significantly different lensing cross sections.

To investigate this, we compute the change in total lensing cross-section with respect to the fiducial case with $\gamma_{\text{dm}} = 1$ when varying ρ_0 and/or r_s to preserve M_{180} . The results are summarised in Fig. 1 for both the lower (top) and higher (bottom) mass scale. The curves in the left panels show the relative difference in unbiased cross-sections, while the curves in the right panels are for biased cross-sections with a limiting luminosity of $4L_*$ (see Section 5.4 below). The solid curves show the relative difference in cross-section when both r_s and ρ_0 are kept fixed when changing the inner slope away from the fiducial value $\gamma_{\text{dm}} = 1$, i.e., not preserving the virial mass M_{180} . The dotted and dashed curve show the difference when preserving M_{180} by varying either ρ_0 (fixing r_s) or r_s (fixing ρ_0), respectively.

The results for the unbiased and biased cross-section are similar. At $\gamma_{\text{dm}} = 0.5$, the offsets between the solid, dotted and dashed curves corresponding to the three different normalisations are marginal, which is expected since for a shallower slope the contribution of the dark matter component decreases with respect to the stellar component which we

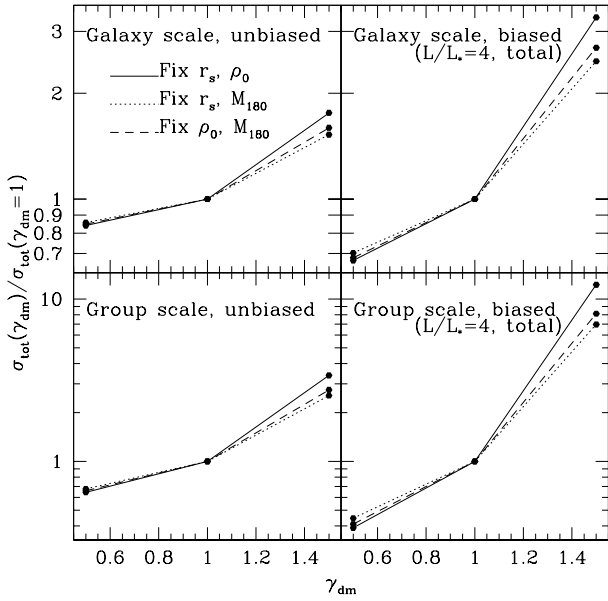


Figure 1. Variation in total lensing cross-section for different normalisations for the lower, galaxy (top) and higher, group (bottom) mass scale. The change in cross-section is shown relative to that of the fiducial case with dark matter inner slope of $\gamma_{\text{dm}} = 1$. The panels on the left show the relative difference in unbiased cross-sections, while the panels on the right are for biased cross-sections with a limiting luminosity of $4L_*$ (see Section 5.4 for details). The solid curves show the relative difference in cross-section when both r_s and ρ_0 are kept fixed, while the dotted and dashed curve show the difference when preserving M_{180} by varying ρ_0 (fixing r_s) or r_s (fixing ρ_0), respectively.

keep fixed. However, the dark matter contribution becomes important when $\gamma_{\text{dm}} = 1.5$, in particular for the high-mass scale as can be seen from the different scaling of the vertical axes. We see that in all cases the solid curve leads to higher cross-sections than the dotted and dashed curve when we preserve M_{180} , which is expected given the increase in mass of tens of per cent.

The latter two normalisations result in changes in the cross-section of which the relative difference is well within the combined statistical and systematic uncertainty in the cross-sections (i.e., while we have attempted to make these models fairly realistic, there are some systematic uncertainties, so we do not trust them to per cent level precision). This implies that varying ρ_0 and/or r_s to preserve M_{180} does not change the lensing properties in a way that is significantly different. In what follows we choose to fix r_s (and hence the concentration r_{180}/r_s), because it is simpler and in line with preserving the (weak) concentration-mass relation for dark matter halos (e.g. Bullock et al. 2001) and the size-luminosity relation for early-type galaxies (e.g. Shen et al. 2003; Bernardi et al. 2007), as discussed further in Section 4.5.2 below.

4.3.3 Intrinsic profiles

For the spherical density profiles, we present a set of plots showing various quantities for both mass scales. We begin

with Fig. 2, which shows the intrinsic, 3d mass density profile $\rho(r)$ for the cusped density profiles (NFW plus Hernquist), for both mass scales. It is apparent that for $\gamma_{\text{dm}} = 0.5$ and $\gamma_{\text{dm}} = 1$ density profiles (stellar plus dark matter), the dark matter component is negligible for scales below ~ 2 kpc for both mass scales, whereas the $\gamma_{\text{dm}} = 1.5$ models have significant contributions from dark matter for all scales shown. The difference between these cases is somewhat reduced when considering the profiles in projection along the line-of-sight, due to the dominant dark matter contributions at large intrinsic radius. Nonetheless, we expect a significant break in the strong lensing properties going from $\gamma_{\text{dm}} = 1$ to $\gamma_{\text{dm}} = 1.5$.

The colour curves in Fig. 2 show the effects of AC on the cusped, $\gamma_{\text{dm}} = 1$ density profiles. We can see (bottom-left panel) that for the lower mass scale, which has a higher ratio of stellar to halo mass, AC tends to increase the density on scales below ~ 10 kpc by ~ 40 per cent depending on the model used, at the expense of a slightly decreased density (~ 3 per cent) for larger scales. For the higher mass scale (bottom-right panel), the density below 10 kpc tends to increase by ~ 30 per cent for the Gnedin et al. (2004) AC prescription, again at the expense of a percent-level decrease on much larger scales.

Fig. 3 shows the negative logarithmic slope $\gamma(r)$ of the intrinsic mass density for both mass scales. We can see that for the individual components of the models, the logarithmic slopes behave smoothly according to equation (12), but for the full model, there can be complex, non-monotonic behaviour. The latter “wiggle” in Fig. 3 is stronger for the cusped than the Sérsic density profiles, reflecting the break in the cusped density profile while the Sérsic density profile turns over smoothly.

The intrinsic profiles of our galaxy models are consistent with the total mass density profile derived by Gavazzi et al. (2007), based on a joint strong-lensing and weak-lensing analysis of 22 early-type galaxies from the SLACS sample. The inferred intrinsic density profile (their Fig. 8b) has an amplitude which falls in between our lower-mass galaxy and higher-mass group scale (for an adopted Hubble constant $h = 0.72$). Moreover, the corresponding slope matches very well the wiggle in the logarithmic slope of our models in Fig. 3. Since this non-monotonic variation is around a value of $\gamma = 2$ (indicated by the dashed horizontal line in Fig. 3), our models as well as the total mass density inferred by Gavazzi et al. (2007) are rather close to isothermal over a large radial range around the Einstein radius. However, the density overall is *not* consistent with isothermal, with clear deviations at small and large radii, which happen well within the two-decade radial range for which Gavazzi et al. (2007) claim consistency with isothermal. We discuss this “isothermal conspiracy” further when studying the profiles in projection next.

4.3.4 Projected profiles

In addition to the plots of the intrinsic, 3d profiles, we also show projected, 2d quantities, which are observationally more relevant. Fig. 4 shows the surface mass density Σ as a function of the projected radius R' , in physical units (kpc) and at the top in angular units (arcsec) for a lens galaxy at the fiducial redshift of $z_L = 0.3$. The total (dark

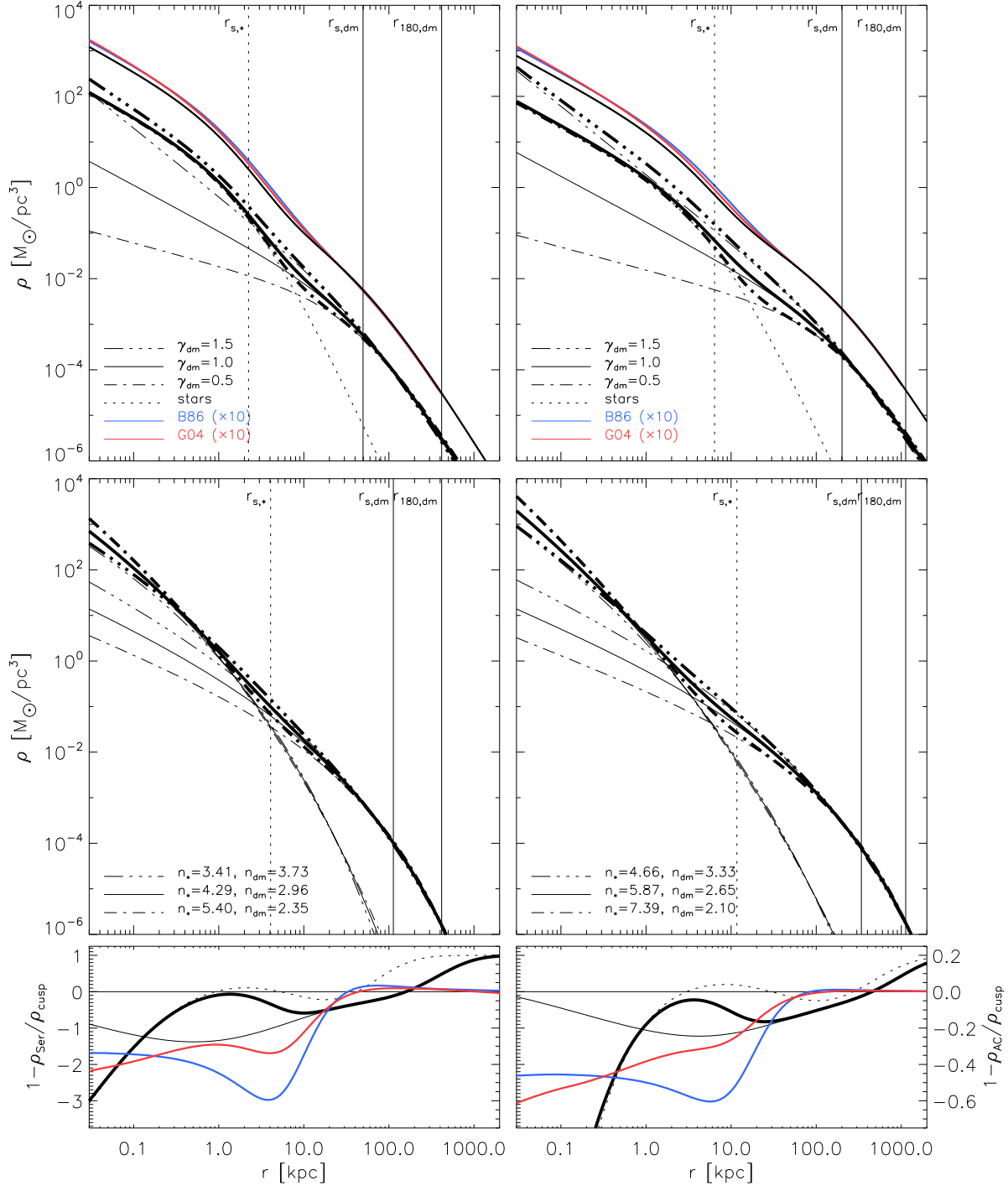


Figure 2. Intrinsic mass density versus intrinsic radius for cusped (top) and deprojected Sérsic (middle) density profiles, for the lower (left) and higher (right) mass scale. Top panels: The dotted curve is the Hernquist profile of the stars, while the single-dot-dashed, solid and triple-dot-dashed curves represent the generalised NFW dark matter profiles with inner slopes γ_{dm} of 0.5, 1.0 (NFW) and 1.5, respectively. The corresponding thick curves show the total mass density profile by combining that of the stars and dark matter. The blue and red curves show the total mass density profile (increased by a factor ten for clarity) taking into account adiabatic contraction (AC) of the fiducial cusped (NFW) dark matter profile (shown as black curve for comparison) using the prescriptions of Blumenthal et al. (1986) and Gnedin et al. (2004), respectively. Middle panels: The thin curves indicate the stellar and dark matter profiles which combined yield the thick curves. The solid curves are based on the fiducial Sérsic indices for both components, whereas the two other curves indicate the variation in the mass density when adopting the limits in n_{dm} and n_* (see Section 4.5). Bottom panels: The black curves show the relative difference in the cusped and deprojected Sérsic mass densities for the stellar component (dotted), dark matter component (thin solid) and the combination (thick solid), using the fiducial density profile parameters. The blue and red curves show the relative difference between fiducial cusped dark matter profile and those after taking into account AC, with corresponding axis labels on the right side. The dotted vertical line indicates the scale radius $r_{s,*}$ of the stellar component, whereas the innermost and outermost solid vertical lines show respectively the scale radius $r_{s,\text{dm}}$ and virial radius $r_{180,\text{dm}}$ of the dark matter component, using the fiducial density profile parameters.

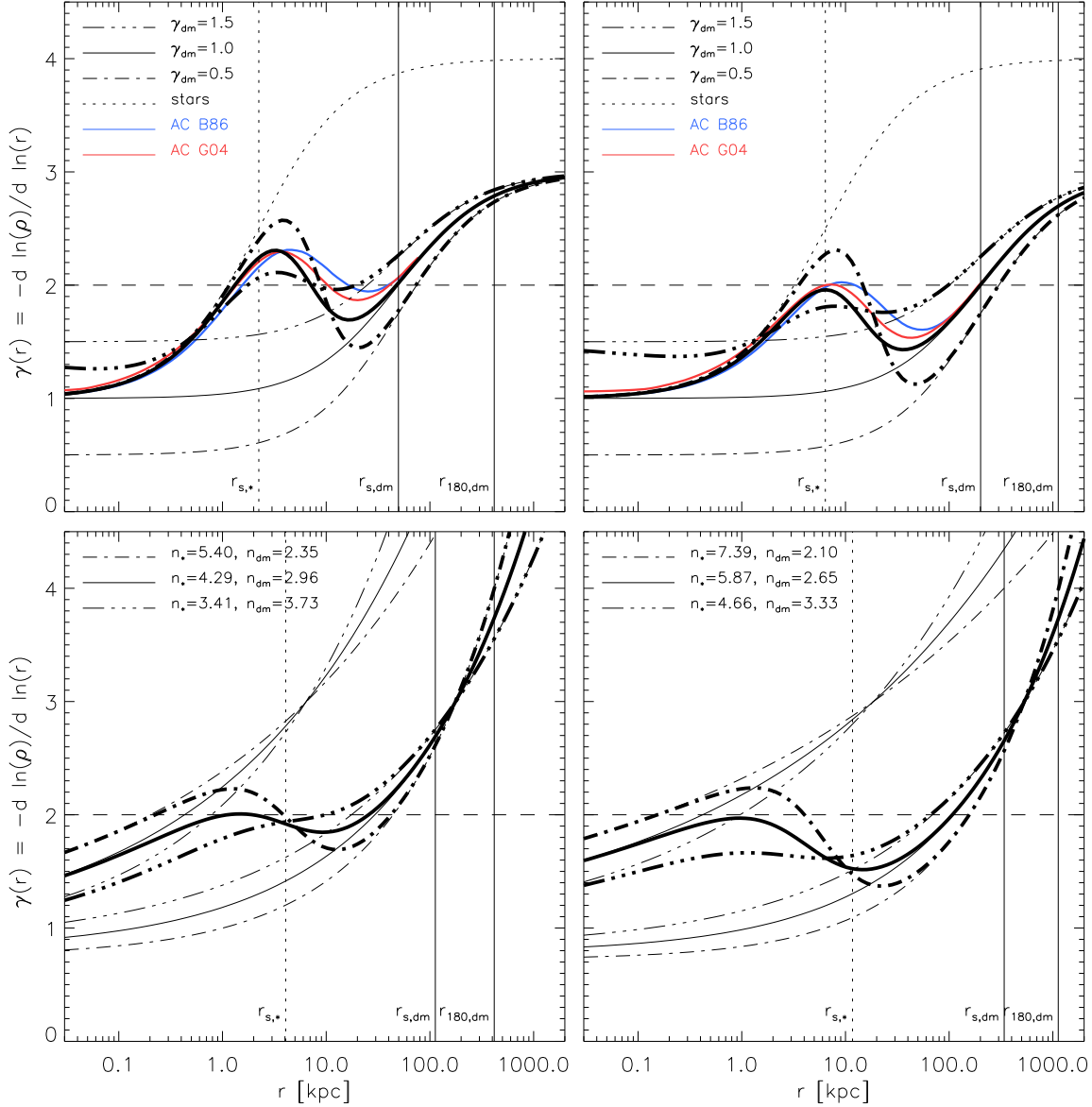


Figure 3. The negative logarithmic slope of the intrinsic mass density as a function of the intrinsic radius, for cusped (top) and deprojected Sérsic (middle) density profiles, and the relative difference (bottom), for the lower (left) and higher (right) mass scale. The horizontal dashed line indicates the slope of an isothermal density profile. The meaning of the other curves is the same as in Fig. 2.

matter plus stars) $\Sigma(R')$ for $\gamma_{\text{dm}} = 0.5$ and $\gamma_{\text{dm}} = 1.0$ are nearly identical and star-dominated for $R \lesssim 1$ kpc. As anticipated, this is a smaller transverse scale than that for which they are identical in 3d.

The colour curves in Fig. 4 show the effect of AC on the projected cusped, $\gamma_{\text{dm}} = 1$ density profiles. As expected, the projection effects have brought in larger scales where AC is less significant, so the projected profiles with AC tend to be higher by ~ 30 (lower mass scale) and ~ 25 (higher mass scale) per cent on the scales of interest (a few kpc for the lower mass scale, ~ 10 kpc for the higher mass scale).

Fig. 5 shows the negative logarithmic slope of the surface mass density, $\gamma'(R')$. If the density profile were a pure power-law, the 2d and 3d negative logarithmic slopes would be related by $\gamma' = \gamma - 1$. Comparing Fig. 5 to Fig. 3, we

see that this simple relation does hold at small and large radii for our cusped models, since these models are asymptotically power-laws. However, it is not valid at intermediate radii, because our models — especially the full models containing both stellar and dark matter components — are far from being simple power-laws. This is particularly notable in the vicinity of the Einstein radius, where the 3d slope varies much stronger with radius than the 2d slope.

Fig. 6 shows the projected dark matter fraction f'_{dm} within projected radius R' . As shown, by varying the dark matter inner slope in the cusped models, we are able to explore models with widely varying fractions of dark matter. The dark matter fractions in our models are consistent with the range of values inferred from attempts to compare stellar and dark matter masses in observed lens systems

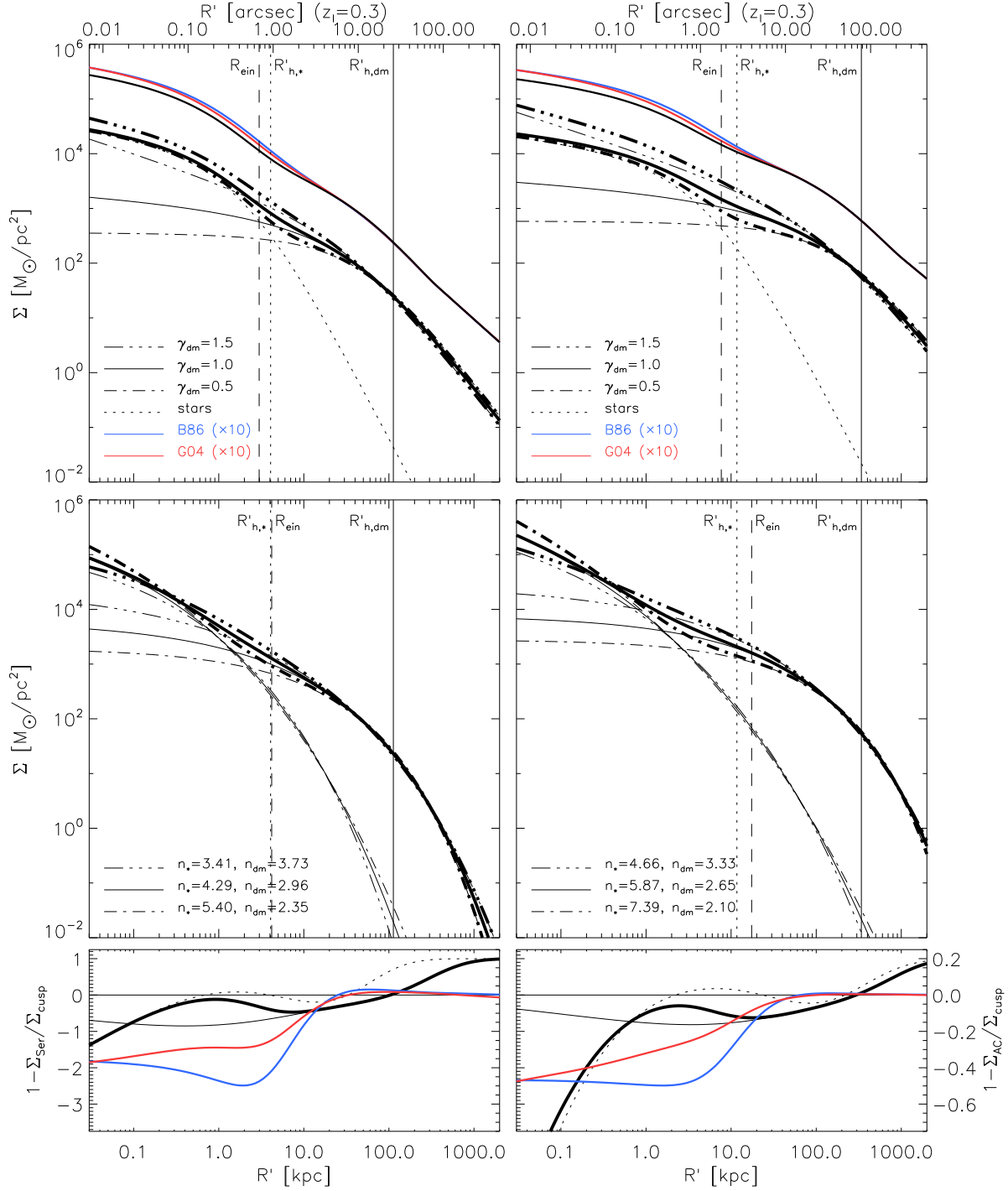


Figure 4. Projected (or surface) mass density versus projected radius, for cusped (top) and deprojected Sérsic (middle) density profiles, and the relative difference (bottom), for the lower (left) and higher (right) mass scale. At the top, projected radius is given in angular units for a (lens) galaxy at the fiducial redshift of $z_L = 0.3$, corresponding to an angular diameter distance of $D_L \simeq 900$ Mpc. With a source at redshift $z_S = 2.0$, the vertical dashed lines indicate the Einstein radii R_{ein} for the composite cusped and deprojected Sérsic models, using the fiducial density profile parameters. The dotted and solid vertical line indicate the half-mass radii $R'_{h,*}$ and $R'_{h,dm}$ containing half of the total mass of the stellar component and half of the virial mass of the dark matter component, respectively. In case of a constant mass-to-light ratio, $R'_{h,dm}$ is equal to the effective radius R_e of the surface brightness. The meaning of the curves is the same as in Fig. 2.

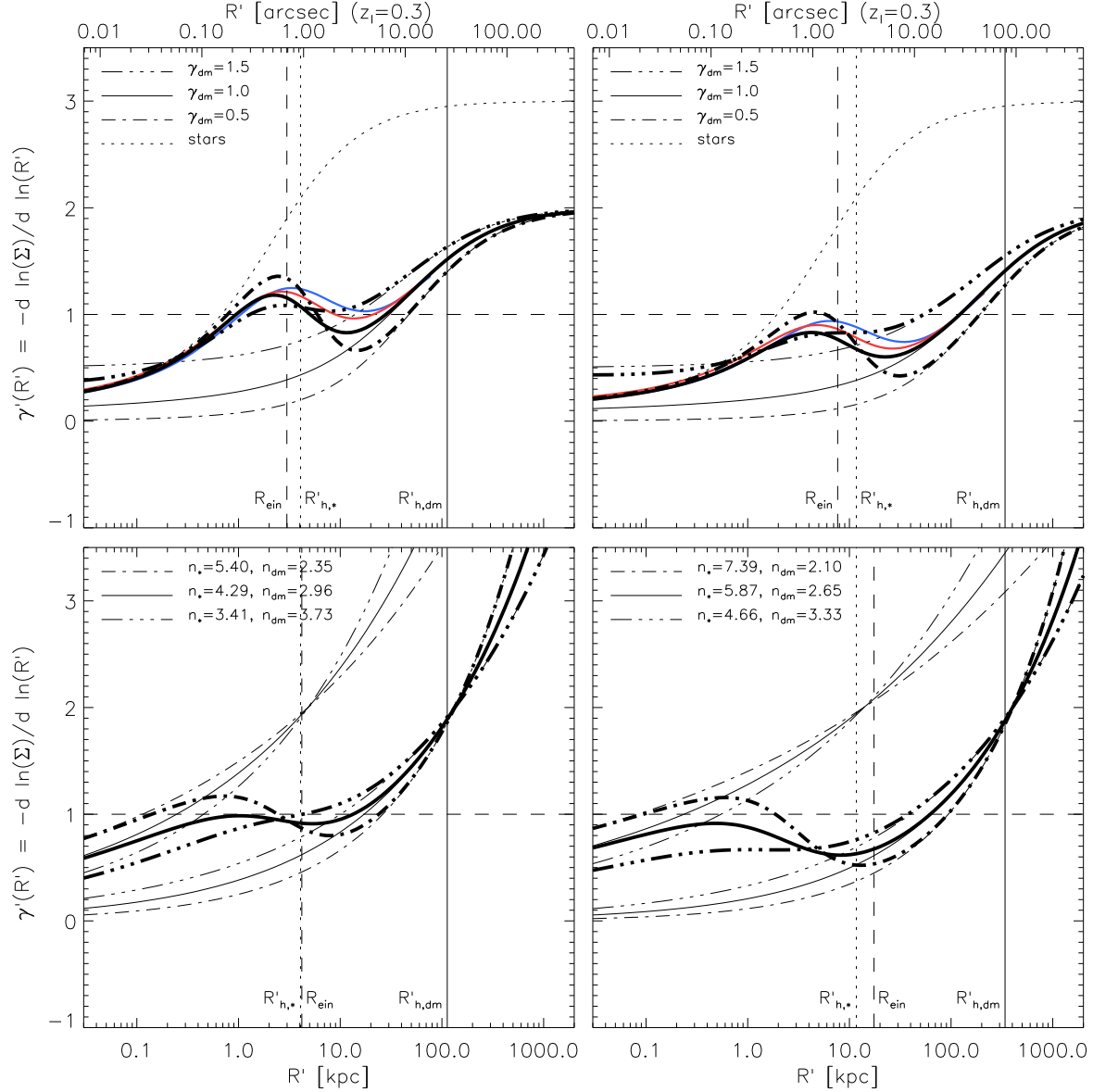


Figure 5. The negative logarithmic slope of the surface mass density as a function of the projected radius, for cusped (top) and deprojected Sérsic (middle) density profiles, and the relative difference (bottom), for the lower (left) and higher (right) mass scale. The horizontal dashed line indicates the slope of a (projected) isothermal density profile. The meaning of the other curves is the same as in Fig. 4.

(Rusin et al. 2003; Rusin & Kochanek 2005; Ferreras et al. 2005; Bolton et al. 2008b).

Finally, Fig. 7 shows the deflection angle $\alpha(R') = d\phi/dR'$ as function of the projected radius R' . The Einstein radii follow from the solution of $\alpha(R_{ein}) = R_{ein}$, which corresponds to the intersections of the dashed one-to-one line with the thick curves, indicated by the filled circles. The corresponding Einstein radii appear at about the half-mass radius $R'_{h,*}$, which in case of a constant stellar mass-to-light ratio corresponds to the effective radius R_e .

Figs. 5 and 7 contain an important point related to attempts to combine strong lensing and stellar dynamics to measure the density profile in the vicinity of the Einstein radius (e.g., Treu & Koopmans 2004; Koopmans et al.

2006). The slope of the composite surface mass density for models with γ_{dm} of 0.5, 1.0 and 1.5 are all close to unity near the Einstein radius. For the lower-mass scale (top-left panel) there is a little more spread around a somewhat higher value $\gamma' \simeq 1.2 \pm 0.2$ than for the higher-mass scale (top-right panel) with $\gamma' \simeq 0.9 \pm 0.1$. However, all are close to the slope $\gamma' = 1$ of a projected isothermal density as indicated by the horizontal dashed line in Fig. 5. In Fig. 7, the deflection angle for the higher-mass scale (top-right panel) increases slowly with radius around the Einstein radius, but for the lower-mass scale the curves are nearly flat around (and beyond) R_{ein} , similar to a constant deflection angle in case of an isothermal density. Even though the stellar density and dark matter density with different

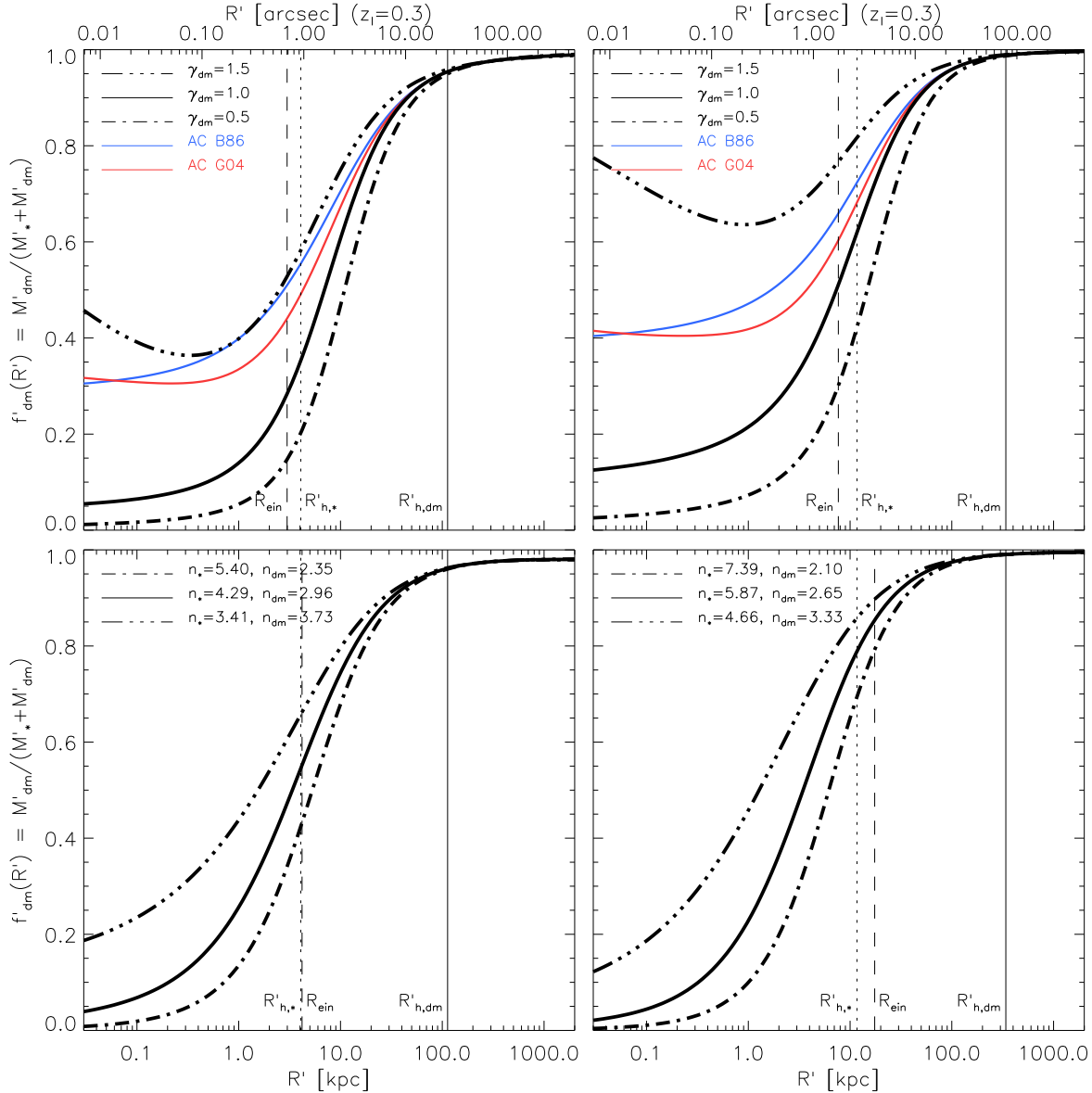


Figure 6. The fraction of projected dark matter within a projected radius, for cusped (top) and deprojected Sérsic (middle) density profiles, and the relative difference (bottom), for the lower (left) and higher (right) mass scale. The meaning of the curves is the same as in Fig. 4.

inner slopes are clearly non-isothermal, the combined density has a projected slope and corresponding deflection angle consistent with isothermal around the Einstein radius. This finding implies that it will be challenging to use strong lensing to constrain the dark matter inner slope γ_{dm} for a two-component model without bringing in information from significantly different scales.

We note that the apparent isothermality of our composite models is a completely unintended consequence of the mass models we have chosen, not something we have imposed by design. However, it provides support for the realism of our models, when compared against observations. There is much evidence from strong lensing (especially in combination with kinematics) that early-type galaxies have total density profiles that are approximately isother-

mal in the vicinity of the Einstein radius (e.g., Rusin et al. 2003; Treu & Koopmans 2004; Rusin & Kochanek 2005; Koopmans et al. 2006). The fact that a superposition of non-isothermal stellar and dark matter profiles can produce a total profile that is approximately isothermal over a wide range of scales — known as the “isothermal conspiracy” — is related to the tendency towards flat rotation curves originally used to argue for a dark matter component. Finally, the same set of SLACS lenses can be fit with a single power-law profile that is consistent with isothermal (Koopmans et al. 2006), or by a more physically intuitive combination of a stellar Hernquist profile and a dark matter halo (Jiang & Kochanek 2007). All in all, the quasi-isothermal nature of our models appears to be consistent with interpretations of strong lensing by real galaxies.

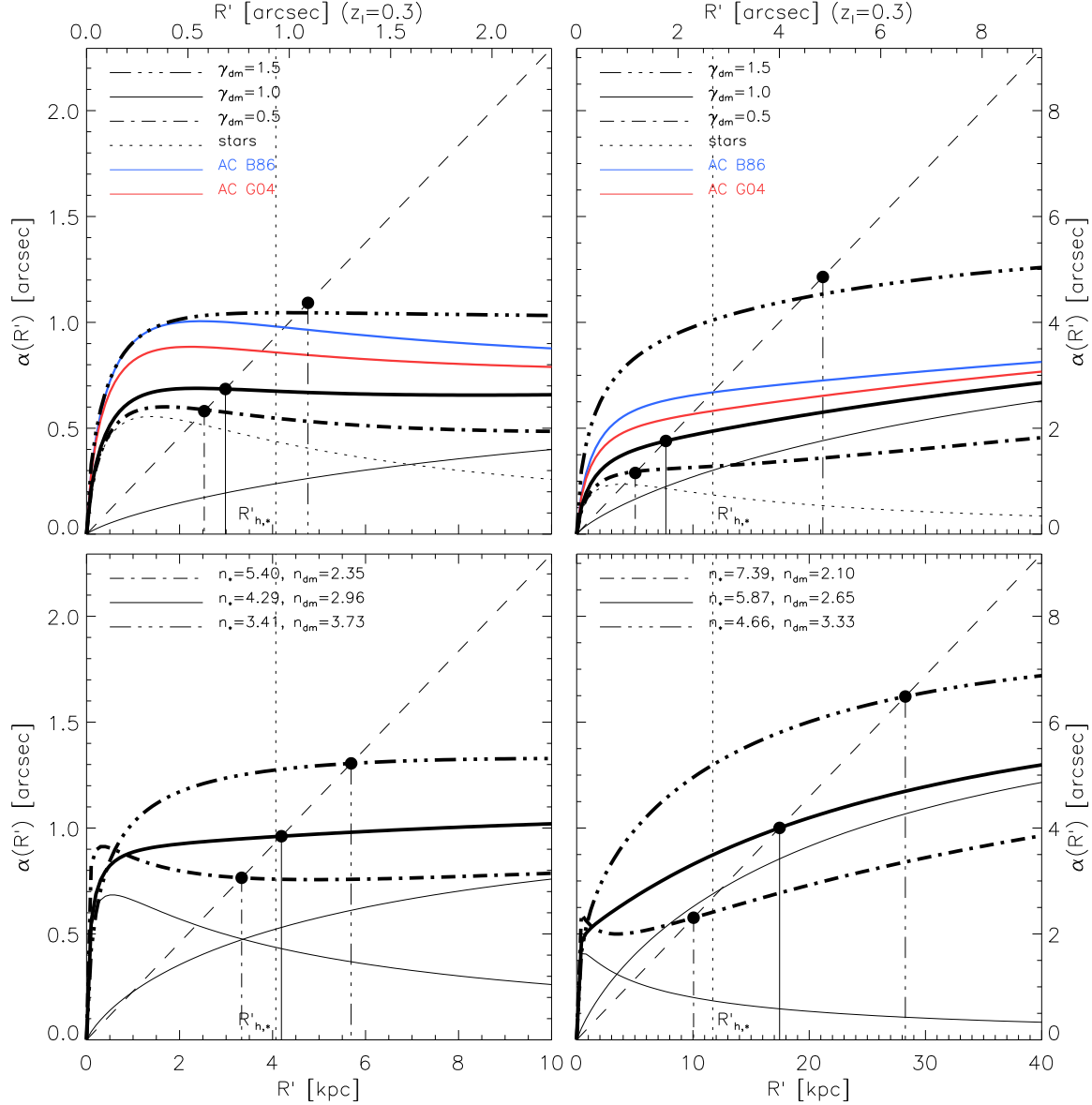


Figure 7. Deflection angle (or derivative of the projected potential) as function of projected radius, for cusped (top) and deprojected Sérsic (middle) density profiles, and the relative difference (bottom), for the lower (left) and higher (right) mass scale. The intersections of the diagonal one-to-one (dashed) line with the (thick) curves of the combined stellar and dark matter components yield the Einstein radii R_{Ein} as indicated by the filled circles and the corresponding vertical lines. The meaning of the other curves is the same as in Fig. 4. The deflection curves of the stellar and dark matter component separately show respectively a strong decrease and increase towards larger radii. However, the combination results for the lower mass scale in an almost flat deflection curve around the Einstein radius and beyond, similar to a constant deflection angle in case of an isothermal density profile.

4.4 Density shape models

We consider seven different models for the shape of the galaxy density: spherical, moderately oblate, very oblate, moderately prolate, very prolate, triaxial, and a mixed model described below. In all but the mixed model, the axis ratios used for the dark matter and stellar components are related in a simple way (see the full description in Section 4.4.1). In all cases the axes of the two components are intrinsically aligned in three dimensions.

4.4.1 Axis ratios

We adopt the mean values $(b/a)_{\text{dm}} = 0.71$ and $(c/a)_{\text{dm}} = 0.50$ from Jing & Suto (2002) for the axis ratios of the triaxial density of the dark matter component. These ratios were determined from cosmological N -body simulations, without any stellar component. We set $(b/a)_{\text{dm}} = 1$ for the oblate shapes, with the same $(c/a)_{\text{dm}} = 0.50$ for the moderately oblate case, and $(c/a)_{\text{dm}} = 0.71 \times 0.50 \simeq 0.36$ for the very oblate case. We set $(b/a)_{\text{dm}} = (c/a)_{\text{dm}}$ for the prolate shapes, with $(c/a)_{\text{dm}} = 0.71$ for the moderately prolate case and $(c/a)_{\text{dm}} = \sqrt{0.71 \times 0.51} \simeq 0.60$ for the very pro-

late case. Note that in the very oblate and very prolate case these choices preserve the product $(b/a)_{\text{dm}} \times (c/a)_{\text{dm}}$ of the triaxial case, and hence the enclosed ellipsoidal mass.

Next, we use results from the cosmological gasdynamics simulations in Kazantzidis et al. (2004) to make a (crude) conversion from the dark matter shape to the rounder shape of the stars: $(b/a)_* = 0.6(b/a)_{\text{dm}} + 0.4$, and similarly for $(c/a)_*$. In practice, in that paper, the axis ratios were a function of separation from the centre of the halo; we neglect those effects in this work. Also, in that work the dark matter halos were themselves made more round due to the presence of baryons, with up to ~ 15 per cent effects out to the virial radius. However, those simulations may suffer from baryonic overcooling, which would tend to accentuate these effects, so we do not incorporate the rounding of the dark matter component at this time.

The final model, the mixed shape model, is constructed using the very oblate stellar shape combined with the triaxial dark matter halo shape. Part of the motivation for doing so is based on the results given by Lambas et al. (1992) for the axis ratio distributions and 3d shapes of early-type galaxies as inferred from the distributions of their projected shapes. In that paper, the elliptical sample containing 2 135 galaxies was found to have a projected shape distribution consistent with a (weakly) triaxial intrinsic shape distribution. Fitting Gaussian distributions in both axis ratios, they found a best-fitting mean and standard deviation of 0.95 and 0.35 in $(b/a)_*$, and 0.55 and 0.20 in $(c/a)_*$. The 4782 S0 galaxies in their sample had a projected shape distribution with best-fit mean value $(b/a)_* = 1$ consistent with oblate axisymmetry, and with best-fitting mean and standard deviation of 0.59 and 0.24 in $(c/a)_*$.

Further motivation is provided by detailed dynamical models of nearby elliptical and lenticular galaxies that accurately fit their observed surface brightness and (two-dimensional) stellar kinematics. These models show that the inner parts of lenticular as well as many elliptical galaxies, collectively called fast-rotators (Emsellem & et al. 2007), are consistent with an oblate axisymmetric shape (Cappellari & et al. 2007). The slow-rotator ellipticals, on the other hand, might be rather close to oblate axisymmetric in the centre but rapidly become truly triaxial at larger radii (van den Bosch et al. 2008, 2008).

We thus consider this mixed model, with a triaxial dark matter shape as in cosmological N -body simulations plus an oblate stellar shape as inferred from observations, as being potentially consistent with reality for the lower mass scale. The triaxial shape for both dark matter and stars may be more appropriate for the higher mass scale.

The resulting axis ratios for each shape model, both for the dark matter and stellar component, are given in Table 2. While we do not explore a broad range of axis ratios due to the prohibitive numbers of simulations involved, we can still get some sense of the trend with axis ratio by looking at the changes from spherical to moderately and very oblate or prolate shapes.

4.4.2 Scale lengths for non-spherical density profiles

When constructing the non-spherical density profiles, we fix the concentration to be the same as in the spherical case, but set the scale length a such that the mass within the

Table 2. Adopted axis ratios of the ellipsoidal intrinsic mass density for the dark matter and stellar component for seven different shape models.

Shape	$(b/a)_{\text{dm}}$	$(c/a)_{\text{dm}}$	$(b/a)_*$	$(c/a)_*$
Spherical	1.00	1.00	1.00	1.00
Moderately oblate	1.00	0.50	1.00	0.70
Very oblate	1.00	0.36	1.00	0.62
Moderately prolate	0.71	0.71	0.83	0.83
Very prolate	0.60	0.60	0.76	0.76
Triaxial	0.71	0.50	0.83	0.70
Mixed	0.71	0.50	1.00	0.62

ellipsoidal virial radius $m_{180} = r_{180}/a$ is equal to the virial mass M_{180} . This is done using

$$a^3 (b/a) (c/a) = r_s^3. \quad (32)$$

In this case, the length scale of the halo is rescaled while maintaining its concentration r_{180}/r_s .

4.4.3 (Mis)alignment of projected axes

We assume that the intrinsic axes of the stellar and dark matter component are aligned. For the axisymmetric models this means that the minor and major axes of the surface mass densities of the stars and dark matter are aligned as well. However, in case of a triaxial dark matter component the projected axes are misaligned with respect to those of the intrinsically rounder stellar component.

The misalignment $\Delta\psi = |\psi_{\text{dm}} - \psi_*|$ follows from equation (2) for the different intrinsic axis ratios of the dark matter and stellar component (Table 2) as a function of the polar and azimuthal viewing angles (ϑ, φ) . The left panels of Fig. 8 show the resulting $\Delta\psi$ for the triaxial (top) and mixed (bottom) shape model. Depending on the viewing direction, the projected axis ratios of the stars and dark matter can become completely orthogonal ($\Delta\psi = 90^\circ$). At the same time, however, the projected ellipticity of the stars $1 - (b'/a')_*$ goes to zero, as shown in the right panels of Fig. 8. This means that the stars appear round on the plane of the sky, so that their position angle on the sky is very hard to establish.

Even ignoring the stellar ellipticity, the probability of a significant misalignment is rather small in the case of random viewing directions⁷. For the triaxial shape model only $\sim 1.2\%$ of the area on the viewing sphere leads to misalignments $\Delta\psi \geq 10^\circ$. This number increases to $\sim 50.8\%$ for the mixed shape model, but at the same time the area on the viewing sphere that leads to a round appearance of the stars is also larger: $\sim 8.3\%$ of the area has $(b'/a')_* \geq 0.95$, while this is only $\sim 2.1\%$ for the triaxial shape model.

Our use of models that lead to almost no situations with significant projected ellipticity *and* misalignment of DM and stellar components is consistent with studies of relatively isolated lens systems, for which the position angles of the light and of the projected total mass agree to within $\lesssim 10^\circ$ (Keeton et al. 1998; Kochanek 2002a;

⁷ We show in Paper II that there is a selection bias in orientation for non-spherical lens galaxies.

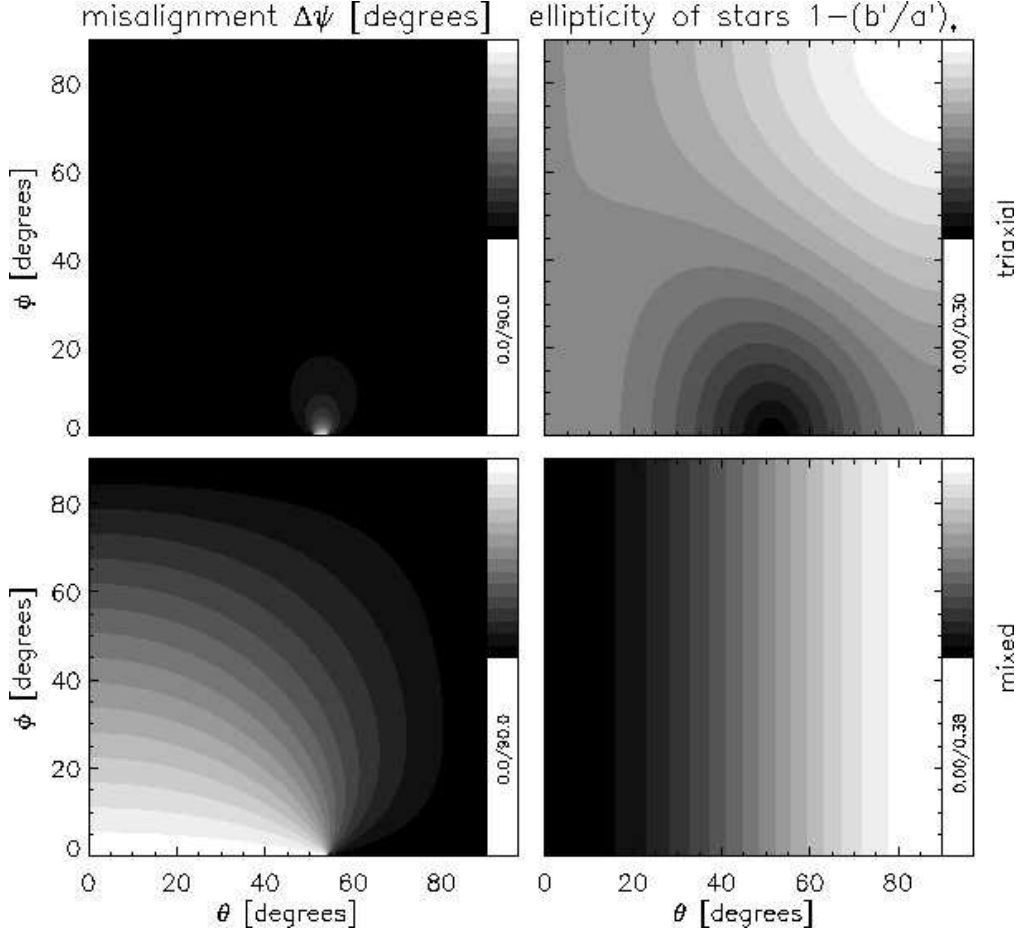


Figure 8. The left panels show the misalignment $\Delta\psi$ between the projected axes of the surface mass density of the stellar and dark matter component of the triaxial (top) and mixed (bottom) shape models, as a function of the polar viewing angle ϑ and azimuthal viewing angle φ . In practice, $\Delta\psi$ is estimated from modelling of the lensing images and the position angle of the stars on the sky. The latter becomes very uncertain if the stars appear too round on the plane of the sky, i.e., in case of a very small ellipticity $1 - (b'/a')_*$ shown in the right panels. Note that these are not equal-area plots since the horizontal axis is θ rather than $\cos\theta$.

Koopmans et al. 2006; Bolton et al. 2008b). Moreover, both the observed surface brightness and stellar kinematics of early-type galaxies are well-fitted by dynamical models with the intrinsic density parametrised by multiple (Gaussian) components that have different shapes but are all co-axial (e.g. Emsellem et al. 1994; Cappellari & et al. 2006). This includes the photometric and kinematic twists observed in particularly the giant ellipticals (van den Bosch et al. 2008, 2008).

The above is all empirical evidence in favour of an initial guess involving a high degree of alignment. While there are many reasons why these assumptions are not perfect, here we do not explore the effects of intrinsic misalignment between the shapes, because of the enormous amount of parameter space involved. Future work should explore this issue further, as well as the issue of warps in the intrinsic and/or projected profiles.

4.5 Deprojected Sérsic simulations

In addition to the simulations with cusped density profiles, we also create a set of simulations with deprojected Sérsic density profiles (Section 2.5), which also provide a good de-

scription of both stars and dark matter over a range of mass scales (Section 2.3). As before, we choose the different parameters for the dark matter and stellar density to create observationally realistic galaxy models.

4.5.1 Density parameters

For the total mass of the stellar component we use the same values given in Table 1 for the lower and higher mass scales. Even though the total mass of the dark matter component is also finite in this case, we adopt for consistency the same virial mass scale by setting the mass within the virial radius $r_{180,\text{dm}}$ equal to $M_{180,\text{dm}}$ as given in Table 1. In spherical geometry, the scale radius of the Sérsic density is the half-mass radius, which for the stellar component is $R'_{h,*}$ given in Table 1. This, in turn, is equal to the effective radius R_e in the case of a constant stellar mass-to-light ratio. For the dark matter component we numerically derive the radius $R'_{h,\text{dm}}$ that encloses a projected mass that is half of the virial mass $M_{180,\text{dm}}$ of the spherical NFW dark matter halo, and use the same half-mass radius for the deprojected Sérsic profiles. This procedure results in $R'_{h,\text{dm}} = 2.2699 r_{s,\text{dm}} \simeq 112 \text{ kpc}$

and $R'_{h,\text{dm}} = 1.6882 r_{s,\text{dm}} \simeq 339$ kpc for the lower and higher mass scale, respectively

The only parameter left to choose is the Sérsic index n . To derive the Sérsic indices n_* of the stellar component, we use the relation $\log n_* = -0.10(M_B + 18) + 0.39$ for Virgo early-type galaxies as derived by Ferrarese & et al. (2006). A luminosity of L_* corresponds to an absolute Johnson B -band and SDSS r -band magnitude of about $M_{B*} = -19.4 + 5 \log(h = 0.72) = -20.1$ (Faber & et al. 2007) and $M_{r*} = -20.28 + 5 \log(h = 0.72) = -21.0$ (Blanton & et al. 2003), respectively. With $B - r = 1.32$ as a typical colour for elliptical galaxies (Fukugita et al. 1995), this means that our choice for the lower and higher mass scales of $\sim 2L_*$ and $\sim 7L_*$ in the r -band translate to $\sim 1.3L_*$ and $\sim 4.7L_*$ in the B -band, or about $M_B = -20.4$ and $M_B = -21.8$. We thus obtain Sérsic indices $n_* = 4.29$ and $n_* = 5.87$ for the stellar component of the lower and higher mass scale, respectively. For the dark matter component, we use the Sérsic fits to simulated Λ CDM halo profiles presented in Merritt et al. (2005). Taking into account the difference in virial mass definition, we obtain $n_{\text{dm}} = 2.96$ and $n_{\text{dm}} = 2.65$ for the lower and higher mass scales, respectively.

In addition to these fiducial Sérsic indices, we also consider values consistent with the observed scatter. For a given absolute luminosity M_B , the scatter in the observed $\log n_*$ in Ferrarese & et al. (2006) is approximately ± 0.1 dex. This scatter results in a range in n_* of [3.41, 5.40] and [4.66, 7.39] for the lower and higher mass scales, respectively. Similarly, for a given virial mass M_{180} , the range of fitted $\log n_{\text{dm}}$ in Merritt et al. (2005) is approximately covered by ± 0.05 dex. Since these findings are based on a low number (19) of simulations, we consider indices ± 0.10 dex around the fiducial values. This scatter implies a range in n_{dm} of [2.35, 3.73] and [2.10, 3.33] for the lower and higher mass scales, respectively.

4.5.2 Normalisation

For the cusped density profiles in Section 4.3.2, changing the dark matter inner slope from the fiducial value $\gamma_{\text{dm}} = 1$ only affects the inner parts of the density profile. As a result, the corresponding change in virial mass $M_{180,\text{dm}}$ (about -20% and $+30\%$ when changing to respectively $\gamma_{\text{dm}} = 0.5$ and $\gamma_{\text{dm}} = 1.5$), could easily be compensated by changing the density amplitude ρ_0 and/or the scale radius r_s . For the deprojected Sérsic density profiles, changing the index n affects the whole density profile rather than just the inner parts, so that the corresponding changes in the mass are much larger. Changing the fiducial dark matter index n_{dm} to the limits of the adopted range (while keeping n_* fixed), results in a factor ~ 3 change in the virial mass $M_{180,\text{dm}}$ for both mass scales. Changing the fiducial stellar index n_* to the limits of the adopted range, results in a factor > 100 change in the total stellar mass $M_{\text{tot},*}$. Preserving the mass thus requires very large variations in the central density ρ_0 and/or the half-mass radius R'_h .

Certainly for the stellar component, changing R'_h is not an option, since early-type galaxies obey a size-luminosity relation (e.g. Shen et al. 2003; Bernardi et al. 2007). Although there is some freedom due to scatter in this relation and the stellar mass-to-light conversion, this relation excludes larger variations in $R'_{h,*}$ when preserving $M_{\text{tot},*}$. A similar conclusion is reached based on the Kormendy

(1977) relation $\langle I_e \rangle \propto R_e^{-0.4g}$, where $\langle I_e \rangle = L_{\text{tot}}/(\pi R_e^2)$ is the mean surface brightness within the effective radius R_e . In case of spherical symmetry and a constant mass-to-light ratio $R'_{h,*} = R_e$ and $L_{\text{tot}} \propto \rho_0 R_e^3 f(n_*)$, where the latter dependence on the Sérsic index follows from equation (15). Therefore, obeying the Kormendy relation means $\rho_0 R_h^{(1+0.4g)} f(n_*) = \text{cnst}$, while preserving the total stellar mass implies $\rho_0 R_e^3 f(n_*) = \text{cnst}$. Since $g \simeq 3$ even at high(er) redshift (e.g. La Barbera et al. 2003; di Serego Alighieri & et al. 2005), these two relations together imply that R_e remains to be approximately constant, while ρ_0 can be varied to compensate for the change in n_* .

A similar scaling relation seems to hold for NFW dark matter halos between their concentration c_{dm} (or scale radius in case of a constant virial radius), and virial mass $M_{180,\text{dm}}$ of the form $c_{\text{dm}} \propto M_{180,\text{dm}}^{-0.13}$ (Bullock et al. 2001). Since the dependence on $M_{180,\text{dm}}$ is weak and the scatter in the relation is rather large, we could not use it before in Section 4.3.2 when changing the inner slope γ_{dm} of the cusped density profile to break the degeneracy between the different normalisation options (which we showed in case of preserving $M_{180,\text{dm}}$ was not necessary, since the effect of the different normalisations on the lensing cross-sections is similar). Salvador-Solé et al. (2007) show that when an Einasto profile is used instead of a NFW profile, a similar concentration-mass relation exists for dark matter halos. Because deprojected Sérsic profiles fit simulated dark matter halos equally well as Einasto profiles (Section 2.3), we expect also in that case a correlation between c_{dm} and $M_{180,\text{dm}}$. As mentioned above, for the Sérsic density the effect of changing n_{dm} is much stronger than changing γ_{dm} for the cusped density, so that varying c_{dm} (while fixing ρ_0) to preserve $M_{180,\text{dm}}$ would violate this concentration-mass relation. As a result, for both the stellar and dark matter component we vary ρ_0 to preserve the (total and virial) mass, while we keep the half-mass radius R'_h fixed.

4.5.3 Density profiles

The profile of the spherical deprojected Sérsic mass density $\rho(r)$ is shown in Fig. 2 in the middle row and compared to the cusped mass density in the bottom row, for the lower and higher mass scales. The thin curves indicate the stellar and dark matter profiles which combined yield the thick curves. The solid curves are based on the fiducial Sérsic indices for both components, whereas the two other curves indicate the variation in the mass density when adopting the above limits in n_{dm} and n_* . In a similar way, we show in Fig. 3 the corresponding negative logarithmic slope $\gamma(r)$, in Fig. 4 the Sérsic surface mass density $\Sigma(R')$, in Fig. 5 the corresponding negative logarithmic projected slope $\gamma'(R')$, in Fig. 6 the projected dark matter fraction $f'_{\text{dm}}(< R')$, and finally in Fig. 7 the deflection angle.

As for the cusped density in Section 4.3.4, we find that both the slope of the composite surface mass density and the deflection angle (Fig. 5 and Fig. 7) are consistent with an isothermal density around the Einstein radius. Especially for the lower-mass scale, the projected slope for all cases converges to $\gamma' = 1$ around R_{ein} , and the curves of the deflection angle are extremely flat at and beyond R_{ein} . As for cusped models, this finding implies that constraints from

strong lensing cannot trivially be extrapolated to smaller and larger radii.

4.6 Computation of surface mass density maps

The lensing properties of a galaxy follow from its surface mass density $\Sigma(x', y')$. For the above galaxy models this is the sum of the surface mass density of the stellar and dark matter components, each of which can be computed as follows. For a given intrinsic shape (a, b, c) seen from a viewing direction (ϑ, φ) , the projected semi-axis lengths (a', b') are given by equations (5)–(7). At each position (x', y') on the plane of the sky, equation (4) then yields the elliptic radius m' . The surface mass density follows by evaluation of equation (3) for a cusped density $\rho(m)$ given in equation (9), or in the case of a Sérsic density directly as $\Sigma(m')$ given in equation (16).

However, rather than doing the numerical evaluation for each position and viewing direction, we instead compute $\Sigma(m')$ on a fine one-dimensional grid in m' , *once* for each intrinsic density profile and shape. We then derive $\Sigma(x', y')$ by linearly interpolating onto this grid at the m' value that (according to equations 4–7) corresponds to the position (x', y') and chosen viewing direction (ϑ, φ) . In particular, in the case of the cusped density, this procedure means that we can avoid doing the numerical evaluation of equation (3) on a two-dimensional grid repeatedly for each viewing direction.

Along with the construction of the cusped and Sérsic galaxy models described above, we implemented and tested this efficient computation of the surface mass density in IDL.⁸ We use a linear grid in m' , except in the inner parts where we sample logarithmically in m' to accurately resolve a central peak in the density. Even so, when we compute the surface mass density on a regular square grid in (x', y') with a given dimension (box size) and sampling (resolution), the resulting fixed pixel size might not be small enough to account for a strong central cusp. This is not the result of the interpolation but is due to the discreteness of the map-based approach. The effects of finite resolution and box size on the surface mass density and corresponding lensing properties are further tested and discussed in Sections 5.7 and 5.8.

We choose the grid in (x', y') such that the x' -axis is aligned with the major axis of the surface mass density of the dark matter component. Even though we assume that the intrinsic axes of the stellar and dark matter component are aligned, in case of a triaxial dark matter component the *projected* axes are misaligned with respect to those of the intrinsically rounder stellar component. As discussed in Section 4.4.3 above, the resulting misalignment angle $\Delta\psi = |\psi_{\text{dm}} - \psi_{\star}|$ follows from equation (2), and depends on the viewing direction (ϑ, φ) . To take this misalignment of the stellar component with respect to the dark matter component into account, we first rotate (x', y') over the misalignment angle $\Delta\psi$

$$\begin{aligned} x_p &= x' \cos \Delta\psi + y' \sin \Delta\psi, \\ y_p &= -x' \sin \Delta\psi + y' \cos \Delta\psi, \end{aligned}$$

and instead of equation (4), we then use $m'^2 = (x_p/a')^2 +$

$(y_p/b')^2$ to define the elliptic radius m' . In case of the axisymmetric models $\Delta\psi = 0$, so that the stellar and dark matter component are always aligned. Finally, we add the maps of the stellar and dark matter components together to arrive at the total surface mass density $\Sigma(x', y')$ of the galaxy model.

In Fig. 9, we show examples of derived surface mass density maps for lower, galaxy-scale mass models with cusped density profiles. The figure includes, from top to bottom, the very oblate mass model viewed close to face-on and close to edge-on, and the mixed shape model. The latter is seen close to the viewing direction that results in the maximum combination of ellipticity of the stars (left column) and misalignment with respect to the dark matter (middle column), resulting in a twist in the combined surface mass density (right column). In Section 5.9 we address the technical issue of how many viewing angles we need to sample in order to accurately characterise how the lensing behaviour changes with viewing direction.

5 LENSING CALCULATIONS

In this section, we describe in detail how we do the lensing calculations necessary for our analysis. We present numerical methods designed to balance efficiency with accuracy (Sections 5.1–5.5), together with extensive tests to validate those methods (Sections 5.6–5.9). All of the calculations described here can be done with GRAVLENS version 1.99k, which is a version of the original software by Keeton (2001b) that has been extended for this project⁹.

5.1 Lens potential, deflection, and magnification

Given the two-dimensional convergence distributions for our models, we need to solve the Poisson equation (22) to find the lens potential. In the present work, we actually need the first and second derivatives of the lens potential (for the deflection and magnification, respectively), and do not work with the potential directly. We use different approaches to obtain the derivatives, depending on the model properties. Note that we apply the methods discussed here to the stellar and dark matter components separately, and construct the composite lens model from a simple linear superposition of the mass components.

If the model has circular symmetry and the convergence is known analytically, the deflection can be obtained from the one-dimensional integral over $\kappa(\theta)$ given in equation (25). Often this integral can be evaluated analytically, so the lens model is fully analytic. This procedure is used for circular deprojected Sérsic models. (For more detail about lensing by circular Sérsic models, see Cardone 2004 and Baltz et al. 2009.)

If the model has elliptical symmetry and the convergence is known analytically, the first and second derivatives

⁹ The features that are new in GRAVLENS v1.99k are identified in the text. All the new features have been tested, and have instructions available through the GRAVLENS `help` command, but are not fully documented in the manual. Version 1.99k can be accessed using the link for latest updates at <http://redfive.rutgers.edu/~keeton/gravlens>.

⁸ <http://www.itervis.com/ProductServices/IDL.aspx>

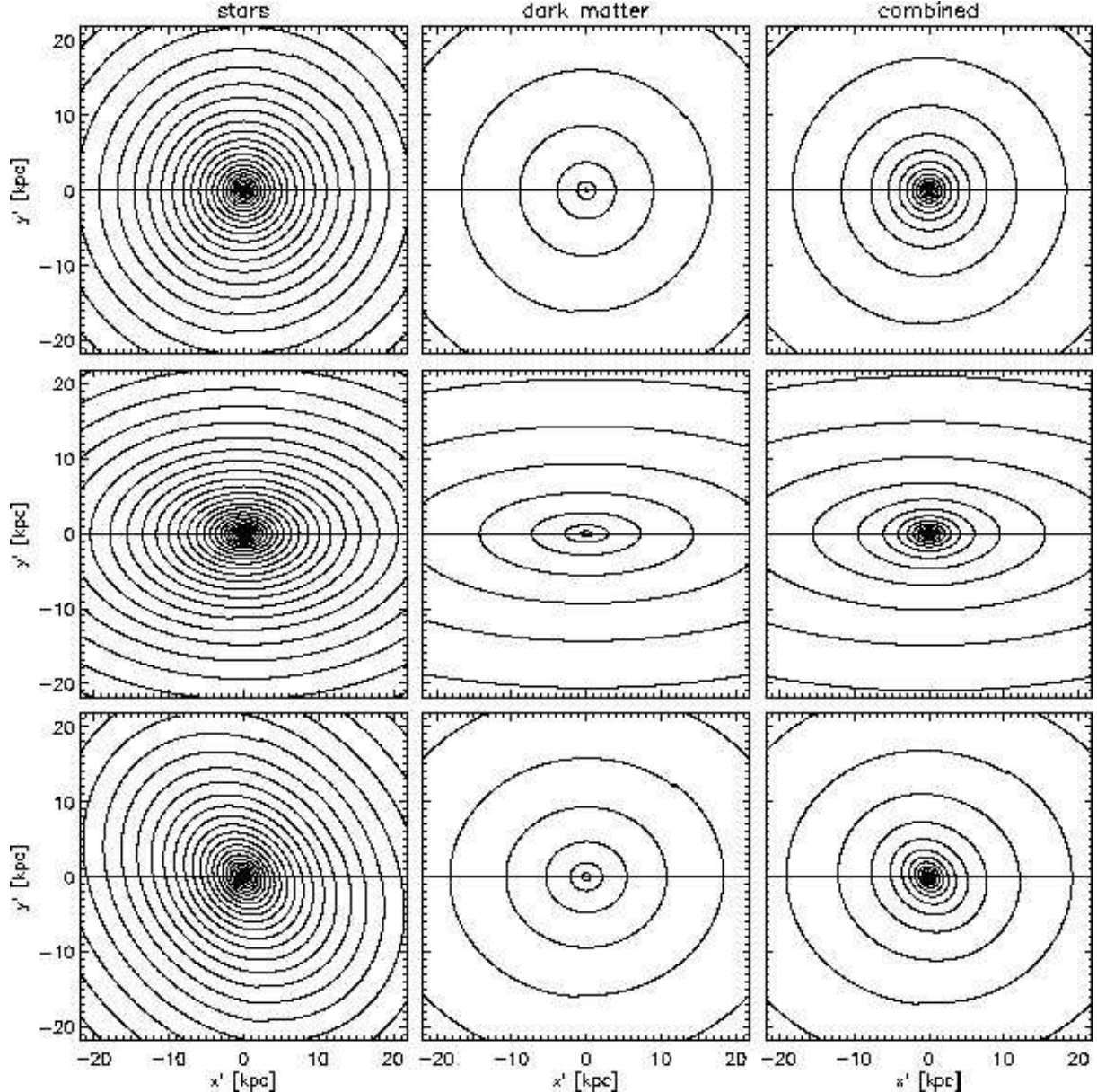


Figure 9. Examples of surface mass density maps Σ as a function of position (x', y') on the sky-plane in case of lower, galaxy-scale mass models with cusped density profiles. From top to bottom, the very oblate mass model viewed close to face-on with inclination $i \simeq 14^\circ$ and close to edge-on with $i \simeq 81^\circ$, and the mixed shape model viewed at a polar angle $\vartheta \simeq 50^\circ$ and azimuthal angle $\varphi \simeq 13^\circ$. The latter is close to the viewing direction that results in the maximum combination of ellipticity of the stars (left column) and misalignment with respect to the dark matter (middle column), resulting in a twist in the combined surface mass density (right column). The contour levels correspond to a factor of ten decrease in Σ going outwards, clearly showing that the stars are more concentrated than the dark matter.

of the lens potential can be obtained from a set of one-dimensional integrals over $\kappa(m')$ and its derivative $d\kappa/dm'$ (Schramm 1990; Keeton 2001a). For elliptical deprojected Sérsic models, we evaluate the integrals numerically,¹⁰ yield-

¹⁰ We note that the steep central profile of Sérsic models can lead to numerical precision requirements that are more stringent than usual. With inadequate precision, there is a systematic and cumulative error that effectively changes the density profile. We achieve the necessary precision by decreasing the GRAVLENS integration tolerance parameter `inttol` from its default value of 10^{-6} down to 10^{-10} .

ing what we call numerical lens models. Circular and elliptical Sérsic models are new features in GRAVLENS that have been added for this project.

For some models, not even the convergence is known analytically, so the projection integral in equation (3) must be evaluated numerically. In such cases we compute the convergence $\kappa(\vec{R}')$ on a map and then solve the Poisson equation using Fourier methods. Here, $\vec{R}' = (x', y')$ is a two-dimensional angular position on the sky in the lens plane, with \vec{k}' its counterpart in Fourier space. We use FFTs to find the Fourier transform $K(\vec{k}')$ of the convergence. We then rewrite the real-space Poisson equation (22) in Fourier

space as

$$-k'^2 F(\vec{k}') = 2K(\vec{k}'), \quad (33)$$

which is readily solved for the Fourier transform $F(\vec{k}')$ of the lens potential $\phi(\vec{R}')$. Derivatives of the lens potential are easily computed in Fourier space: for example, the Fourier transform of $\vec{\nabla}\phi(\vec{R}')$ is $i\vec{k}'F(\vec{k}')$. We can then use inverse FFTs to convert back to real space. All of this analysis can be done with the GRAVLENS routine `kap2lens` (which has been added and tested for this project). We refer to lens models computed this way as map-based lens models, and we use them for our cusped models.¹¹

There are four important technical details to consider in the Fourier analysis. The first issue is avoiding “edge effects” that may arise because we are using a rectangular box with an elliptical density map, and because FFTs naturally impose periodic boundary conditions. We embed the κ -map in a grid at least twice as large as the desired box in each direction (and then round up to the next power of two, as required for FFTs). We take advantage of the fact that our density models have circular or elliptical symmetry, and we know (from Newton’s third law) that the gravitational force inside an elliptical shell due to that shell is zero. We can therefore set the density to zero outside of a reference ellipse that is larger than the region where we wish to study lensing, without affecting the lensing deflections or magnifications (or differential time delays, although we do not study those). Specifically, if the box side length is L , and the angle of the projected mass distribution relative to the x' axis is ψ (see also Section 2.2 and equation 2 in particular), we first define the axes of the projected mass distribution

$$\begin{aligned} x_p &= x' \cos \psi + y' \sin \psi \\ y_p &= -x' \sin \psi + y' \cos \psi \end{aligned}$$

and then set κ to zero when

$$(x_p)^2 + \left(\frac{y_p}{b'/a'}\right)^2 > \left(\frac{L}{2}\right)^2. \quad (34)$$

The second issue arises because equation (33) is ill-behaved at $\vec{k}' = 0$. We avoid this problem by setting all Fourier transforms to zero at $\vec{k}' = 0$. Since $K(0) \propto \int \kappa(\vec{R}') d\vec{R}'$, putting $K(0) = 0$ amounts to requiring that the total mass in the FFT box vanish. That, in turn, means the code effectively adds a negative, uniform mass sheet to offset the positive mass in our model κ -map. We can compensate by explicitly inserting a positive mass sheet to compensate for the effective negative mass sheet. We have carefully tested this approach to verify that it yields accurate lensing calculations (see Section 5.6).

As a third issue, we need to make sure our results are not affected by the resolution of the grid on which we compute κ . Finally, we must necessarily work in a finite box, and we need to check that our results are not affected by the size of the box. We examine the latter two issues carefully below in Sections 5.7 and 5.8, respectively.

¹¹ Hernquist and NFW models could be treated analytically in the spherical case and numerically in the elliptical case, since the convergence is known analytically. However, we must treat generalised NFW models with $\gamma \neq 1$ with the map-based approach, since the convergence is not analytic. We opt to handle all the cusped models in the same way for uniformity.

5.2 Image configurations

The GRAVLENS software features a general “tiling” algorithm to solve the lens equation and find the images of a given source (see Keeton 2001b for details). We can check the recovered images using general considerations from lens theory. First, we classify the images as minima, maxima, and saddle points as discussed in connection with equation (27) in Section 3.1. We can then categorise the image configuration as follows:

- A 2-image lens has one minimum and one saddle point (plus one maximum that we do not analyse).
- A 3-image lens has two minima and one saddle point.
- A 4-image lens has two minima and two saddle points (plus one maximum that we do not analyse).

Note that all three cases satisfy the image number relation in equation (28). Recall from Section 3.1 that we find but do not analyse maximum images because they are rarely observed and do not play a major role in most strong lensing applications.

According to lens theory, these are the only viable multiply-imaged configurations that can be produced by an isolated galaxy whose central surface density is shallower than $\Sigma \propto R'^{-1}$ (see Burke 1981; Schneider et al. 1992). Therefore, any set of recovered images that does not fall into one of these three categories must represent a numerical error.

In general, the error rate in GRAVLENS is very low. The few errors that do occur arise from two causes, which are related to the tiling algorithm. First, when the source lies very close to the caustic, two of the images can lie so close together (straddling the critical curve) that they are difficult for the tiling algorithm to resolve. Second, the tiling algorithm has adaptive resolution, which is valuable but presents certain challenges in regions where the resolution changes (cf. Fig. 4 of Keeton 2001b). In most cases checking the image configuration identifies the rare errors. There is one error that can slip past this check: if the code fails to find one saddle point of a 4-image lens, it will misclassify the system as a 3-image lens. We shall see below (Section 5.9) that this error does occur, but at a low rate that does not corrupt our results at a significant level.

5.3 Point source cross-sections

Our initial focus will be on understanding intrinsic selection biases in strong lensing surveys (see Paper II). We therefore study lensing cross-sections with the idea that any physical effect that enhances the cross-section will be more likely to appear in lens samples, while any effect that reduces the cross-section will be disfavoured. Historically, most lenses found in systematic surveys had point-like images (quasars or radio sources). That is changing with the advent of surveys like SLACS (Bolton et al. 2006, 2008a), but the statistics of galaxy/galaxy strong lensing are much more complicated than the statistics of point source lensing (Dobler et al. 2008), so we currently focus on the point source case.

At the most basic level, the lensing cross-section is just the area of the source plane that leads to multiple imaging. We call this the total cross-section (σ_{tot}), and subdivide it

into the cross-sections for the regions that produce 2, 3, or 4 images (σ_2 , σ_3 , and σ_4). In real surveys, we also need to account for the fact that brighter lensed images are easier to observe; this “magnification bias” effect is discussed in Section 5.4. The cross-sections have dimensions of area on the sky, so the natural unit is arcsec^2 .

We compute the cross-sections using Monte Carlo techniques. We place a source at a random position behind the lens, and solve the lens equation numerically to find all the images of this mock lens. We repeat this process many times, tabulate the number of mock 2-image, 3-image, and 4-image lenses, and use the input number density of sources to compute the associated cross-sections. We find that using 5000 sources provides a good balance between run time and statistical uncertainties.

The most obvious approach is to distribute sources randomly and uniformly in the smallest circle enclosing the lensing caustics in the source plane. However, this approach yields poor sampling of high-magnification systems that are rare but important, especially for magnification bias (see Section 5.4). For an alternate approach, Keeton & Zabludoff (2004) pointed out that picking positions randomly and uniformly in the *image* plane, and then mapping them to the source plane, yields a set of source positions that are random but weighted by the total magnification of all images (see Fig. 10). We must account for the magnification weighting in order to compute the cross-section and magnification bias properly, but that is a straightforward task. Compared with uniform source sampling, magnification-weighted source sampling is no more complicated in concept or algorithm, and yields superior results for Monte Carlo calculations of lensing cross-sections and magnification bias.

We determine the statistical errors on the cross-sections using bootstrap resampling. We create 500 resampled sets of mock lenses, and use the variance among them as the statistical uncertainty. All of this analysis (including bootstrap resampling) can be done with the GRAVLENS routine `mockcsec` (new in version 1.99k).

5.4 Magnification bias

Most lensing surveys have a flux limit that influences the statistical distribution of lenses. The fact that brighter images are easier to observe leads to a lensing “magnification bias” (e.g., Turner et al. 1984). We account for this fact by computing not just the lensing cross-section itself, but the combination of cross-section and magnification bias, which we call the biased cross-section.

Consider a survey in which the number of sources brighter than flux S is $N_{\text{src}}(>S)$, while the survey flux limit is S_0 . The survey is sensitive to systems in which the intrinsic flux S and the lensing magnification μ combine such that $\mu S > S_0$. Thus, the total number of lenses found in the survey has the form of an integral over the source plane,

$$N_{\text{lens}} \propto \int N_{\text{src}}(>S_0/\mu) d\vec{\beta}. \quad (35)$$

This number is divided by the total number of sources to obtain the lensing probability, leading to the following definition for the biased cross-section (Keeton & Zabludoff 2004;

Mitchell et al. 2005; Huterer et al. 2005):

$$\sigma_n = \int_n \frac{N_{\text{src}}(>S_0/\mu)}{N_{\text{src}}(>S_0)} d\vec{\beta} \quad (36)$$

The subscript n indicates that we can compute the biased cross-section for lenses with n images by restricting the integral to the appropriate region in the source plane (cf. Fig. 10). (Note that we do not distinguish between the symbols for unbiased and biased cross-sections, because we have tried to be explicit in the subsequent text about which we are using.) The cross-section can be combined with the number density of sources to obtain the observed number of lens systems.

While magnification bias depends explicitly on the flux limit of a survey, it depends implicitly on the resolution as well. For a survey that detects lenses but does not resolve the images (assuming they are resolved in follow-up observations), the initial detection depends on the combined flux of all images, so it is the total magnification that enters equation (36). For a survey that can resolve the images at the outset, the discovery of lensing depends on the flux of the second-brightest image,¹² so it is the second-ranked magnification that is used in equation (36). To keep our analysis as general as possible, we present results for both cases.

To compute biased cross-sections we must specify the source counts, $N_{\text{src}}(>S)$, or equivalently the differential counts, dN_{src}/dS , near the survey flux limit. We consider optical quasar surveys to determine a reasonable model. For optical surveys, dN/dS is typically modelled as a broken power-law, so we consider the two extremes. Based on the results for SDSS and 2QZ in the g - and i -bands (Croom et al. 2004; Richards & et al. 2006), we find that $d \log N_{\text{src}}/d \log S = \alpha$ where $\alpha \sim 1$ at the bright end and ~ 0.1 at the faint end. This corresponds to

$$\frac{dN_{\text{src}}}{dS} \propto S^{-\nu}, \quad (37)$$

where $\nu = 2.5\alpha + 1$. Thus, our two values of ν are 3.5 and 1.25. (A faint-end slope of $\nu = 1.25$ is consistent with the spectroscopic survey of faint quasars by Jiang & et al. 2006.) To account for the break in the power-law, we implement a functional form commonly used for quasar luminosity functions,

$$\Phi(L) \propto \frac{1}{(L/L_*)^{\nu_1} + (L/L_*)^{\nu_2}} \quad (38)$$

where we use ν_1 and ν_2 of 3.5 and 1.25. For simplicity, we consider limiting luminosities rather than limiting fluxes, but we examine a broad range of values: $0.04L_*$, $0.4L_*$, and $4L_*$ (chosen deliberately to sample the full range of effective slopes with even spacing in magnitude). These correspond to effective slopes ν_{eff} in equation (37) of 1.25, 1.5, and 3.4, although we caution that the luminosity function is far from a pure power-law (especially near the intermediate limiting luminosity), so magnification bias depends not just on ν_{eff} but on the full shape of the luminosity function.

¹² A 2-image system in which one image is fainter than the flux limit will not be identified as a lens. A system with more than two images will be identified as a lens if at least two images are above the flux limit. (If some images are below the flux limit, the true number of images may not be known at first, but the system will still be identified as a lens.)

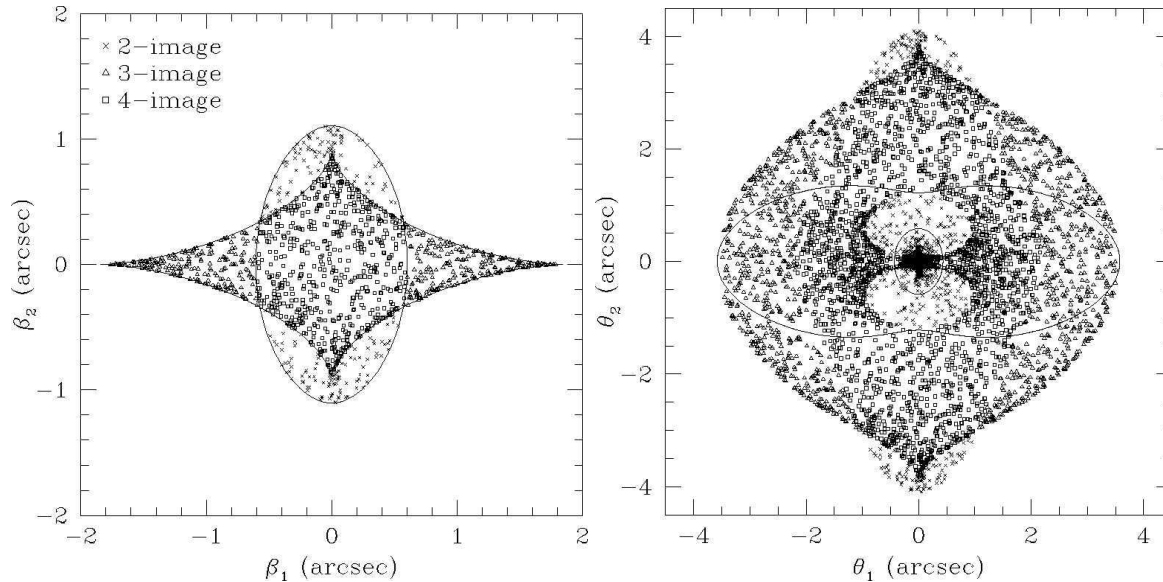


Figure 10. Sample mock lenses for our very oblate higher mass, group scale model viewed edge-on. The left panel shows the caustics in the source plane, along with random source positions selected with magnification weighting (see Section 5.4). The right panel shows the critical curves in the lens plane, along with the images of the random sources. The horizontal axis is aligned with the major axis of the surface mass density of the dark matter component (which in turn is aligned with the stellar component in this axisymmetric case). The point type denotes the number of images, as indicated in the legend. The left panel clearly shows the division of the source plane into 2, 3, and 4-image regions bounded by the caustics. The right panel shows that the lens plane is also divided into distinct regions, although they are not bounded by easy-to-find curves (cf. Fig. 1 of Finch et al. 2002). This figure includes only 2000 sources for clarity, compared with 5000 used in our full analysis.

In summary, we track 7 values of cross-section: the unbiased one, and 6 biased ones (= 2 weighting schemes \times 3 limiting magnitudes). The GRAVLENS routine `mockLF` (new in version 1.99k) can be used to define a double power-law source luminosity function that `mockcsec` uses to compute biased cross-sections.

5.5 Image separation distributions

In addition to the lensing cross-sections, we also consider the distribution of image separations $\Delta\theta$. Here, we define the image separation for a given lensing system as the maximum distance between any two images in the system. This definition is simple and well-defined even for image systems with arbitrary numbers of images, and it has been used before (e.g., Inada & et al. 2003; Oguri & Keeton 2004; Huterer et al. 2005).

In principle, especially for systems with > 2 images, there may be more sophisticated ways to characterise image separations that incorporate information about the full configuration of images. While Kochanek (2002b) and Oguri (2007) have taken first steps in this direction, there has been no systematic exploration of various image separation statistics. We defer consideration of these issues to future work.

5.6 Validation

To validate our Monte Carlo methods for computing lensing cross-sections, we present a simple test case with a singular isothermal sphere lens, for which cross-sections can be computed analytically. For concreteness we set the Einstein

radius to be $R_{\text{ein}} = 1''$ and we consider a simple power-law source luminosity function with $\nu = 1.25$, as appropriate for the faint end of our fiducial broken power-law model. (The biased cross-section cannot be computed analytically for the full broken power-law luminosity function.) The ratio of the numerical to analytic cross-section is 0.988 ± 0.003 for the unbiased cross-section, as well as for the biased cross-section using the total magnification. (The statistical error bar is from bootstrap resampling.) Thus, the numerical cross-sections are accurate to about 1 per cent.

To test our Fourier methods for handling map-based lens models, we present an example using our higher mass scale deprojected Sérsic model. We compute the cross-sections with an analytic circular lens model, now using our fiducial broken power-law source luminosity function and tracking 7 cross-sections (one raw and six biased). We then create a κ -map that is $30''$ on a side and has 800^2 pixels,¹³ and recompute the cross-sections using a map-based lens model. The ratio of the cross-section from the map-based model to that from the analytic model is between 0.960 and 1.041 for all 7 cross-sections. The statistical uncertainties depend on the bias mode, ranging from 0.001 (for the unbiased cross-section) to 0.023 (for the biased cross-section

¹³ The box size is the fiducial value determined from the box size tests discussed in Section 5.8, and the resolution is twice the fiducial resolution discussed in Section 5.7. While we clearly show in that subsection that the fiducial resolution is sufficient for cusped models, we have found that twice better resolution is necessary to resolve the very steep inner parts of the higher mass, deprojected Sérsic model (stellar component).

using the second-brightest magnification and a limiting luminosity of $4L_*$). The ratios become even closer to unity as the resolution increases, but we defer further discussion of the resolution to Section 5.7. The main conclusions we draw from this test are that the Fourier methods are valid and that map-based lens models yield accurate cross-sections.

5.7 Resolution

As noted in Section 5.1, we need to ensure that the lensing properties of our model galaxies are not affected by the resolution of the grid on which we solve the Poisson equation. Here we present convergence tests to determine acceptable pixel sizes. Before designing these tests, we must determine precisely how the pixel size can cause problems with resolution. There are two separate issues: (i) In cases where the Einstein radius is quite small, the finite pixel size may cause GRAVLENS to calculate a polygonal rather than elliptical inner critical curve (in the lens plane), and consequently a polygonal outer source plane caustic as well. (ii) In cases where the inner slope of the density profile is very steep, a large pixel size may mean that its slope, and therefore the location of the inner critical curve, are poorly determined. We consider the two cases separately below.

5.7.1 Obtaining a smooth inner critical curve

For these tests, we use the mass models with $\gamma_{\text{dm}} = 0.5$, since they have the smallest Einstein radii and cross-sections, and therefore yield the most stringent resolution requirements from a standpoint of having a smooth inner critical curve.

We begin with a pixel size of $0.025''$ and $0.075''$ for the galaxy and group scale models, respectively (with $10''$ and $30''$ boxes; see Section 5.8). We vary the pixel size to a factor of 2 smaller, and a factor of 2 and 4 larger in the hopes (a) of seeing that the lensing results have converged by the smallest pixel sizes, and (b) of determining the largest pixel sizes that yield reliable results. We do these tests using a limited set of models: a spherical model, followed by the very oblate, very prolate and triaxial models seen from the most extreme 2, 2, and 3 viewing directions along the principal axes.

The figures of merit for the convergence tests are the lensing cross-sections (σ_2 , σ_3 , σ_4 and σ_{tot} separately), although we also examine the critical curves and caustics. We are interested in cross-sections both with and without magnification bias (according to the various magnification schemes discussed in Section 5.4). For the purpose of this test, we require convergence of the cross-sections at the 5 per cent level.

The effects of resolution are seen qualitatively in the caustics, which are shown in Fig. 11 for three of the eight lens configurations. (Note that the mass density distributions are always elongated along the x' axis, but as usual the caustics are elongated in the perpendicular direction.) The quantitative results of the resolution tests can be summarised as follows:

- For the lower mass scale, the most stringent requirements on the resolution come from the very oblate, edge-on model, for which we require $0.025''$ pixels. Even for this model, the resolution seems to have converged, i.e., the difference between $0.025''$ and $0.0125''$ pixels is much less than

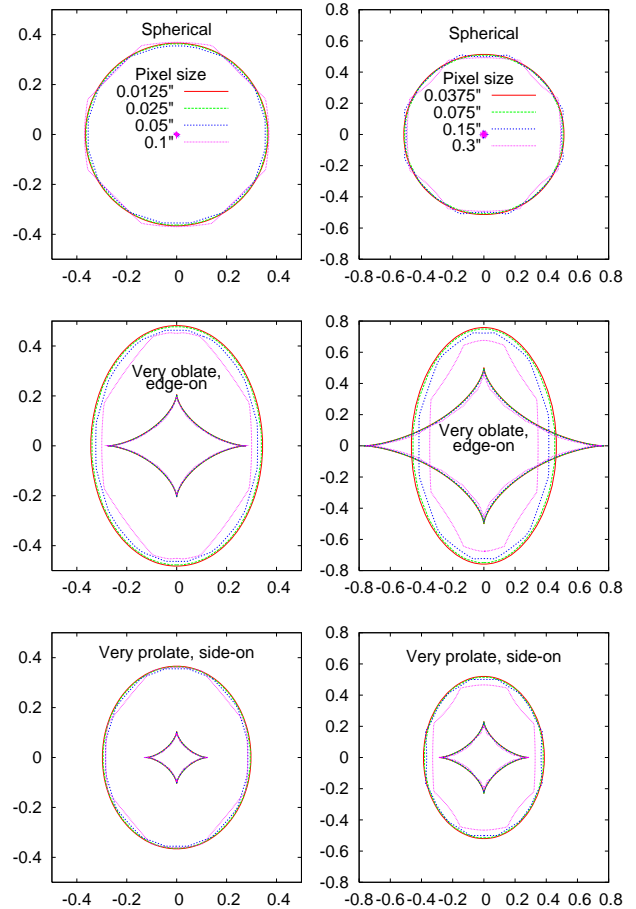


Figure 11. Source plane caustics for the lower (left) and higher (right) mass models with three of the eight extreme lens configurations used for the $\gamma_{\text{dm}} = 0.5$ resolution tests: spherical, oblate (edge-on), and prolate (side-on) from top to bottom. The pixel scales are as labelled on the top plot for each mass scale. The axes are in the plane of the sky (in units of arcsec) with the horizontal axis aligned with the major axis of the surface mass density of the dark matter component.

our 5 per cent convergence criterion. For the very prolate, side-on model, $0.025''$ pixels are formally insufficient for the 4-image cross-section. However, the 4-image cross-section is only ~ 5 per cent of the total cross-section, and with such a small value the statistical uncertainties are large, so the failure is actually marginal and not a significant concern.

- For the higher mass scale, the most stringent resolution test also comes from the very oblate, edge-on case. The second-best resolution ($0.075''$ pixels) marginally satisfies our convergence criterion for the 4-image case, and marginally fails for the 3-image case. However, this marginal failure is unlikely to be too crucial, since the 3-image cross-section is such a small fraction of the total cross-section. In all other cases, the second-best resolution ($0.075''$ pixels) is clearly sufficient at the 5 per cent level.

- In general, as we have predicted, the radial caustic is much more strongly affected by pixelisation effects than the tangential caustic, since the radial caustic maps to the inner critical curve in the lens plane. The radial caustic tends to become more polygonal rather than elliptical as the resolu-

tion is degraded. In Fig. 11, it is clear that the caustics are nearly identical for both the best and second-best resolutions, and that the two poorer resolutions are insufficient.

In conclusion, our second-best resolutions for both mass scales, $0.025''$ ($\simeq 0.11$ kpc) and $0.075''$ ($\simeq 0.33$ kpc), appear to be safe choices from the standpoint of obtaining smooth critical curves and caustics, and the results have converged in comparison with higher resolution simulations at the 5 per cent level. In dimensionless units, these resolutions correspond to ~ 25 pixels lengths per R_{ein} .

5.7.2 Resolving a steep inner slope

The other resolution issue, the ability to resolve the slope of the density profile in the inner regions, is most easily tested using our steepest cusped model, $\gamma_{\text{dm}} = 1.5$. In this case, we repeat the previous tests but only for the spherical case.

Our results suggest that while this effect may be significant for the poorest resolution we consider, the results have converged at better than the 5 per cent level for our fiducial resolution. For example, in the previous subsection (spherical $\gamma_{\text{dm}} = 0.5$ case), the fiducial resolution gave cross-sections that were 1.4 and 2.7 per cent lower than the best resolution (lower and higher mass models, respectively); the poorest resolution led to a highly significant 20 and 35 per cent reduction of the cross-section. For $\gamma_{\text{dm}} = 1.5$, those numbers are 1.1 and 0.9 per cent reduction in σ_{tot} for the fiducial resolution, or 15 and 11 per cent reduction for the poorest resolution. In all cases, these results are for the unbiased cross-section, for which it is clear that the fiducial resolution is sufficient to solve both possible resolution problems. For the biased cross-section, the resolution requirements appear to be slightly less stringent.

While we do not use a map-based approach for the deprojected Sérsic profile simulations, similar convergence tests suggest that such an approach would lead to more stringent resolution requirements (at least a factor of two better), due to the necessity of resolving a very steep inner slope in the innermost regions. The reason these models may be particularly problematic is that they do not converge to a single inner slope, unlike the cusped models.

5.8 Box size

We also need to check that the size of the box in which we solve the Poisson equation does not affect our lensing results. We have again run convergence tests, but now using mass models with $\gamma_{\text{dm}} = 1.5$ since these have the largest Einstein radii and hence the greatest sensitivity to the box size. We include non-spherical models since the elongation of the mass distribution may create extra demands on the size of the box in the direction of the major axis. As in the resolution tests, we use only the extreme non-spherical configurations, as a worst-case scenario.

To begin, we use $10'' \times 10''$ and $30'' \times 30''$ boxes for the galaxy and group scale models, respectively (with our fiducial $0.025''$ and $0.075''$ pixels; see Section 5.7). We then examine box sizes of $5''$, $10''$, and $15''$ for galaxy scale models, and $15''$, $30''$, and $45''$ for group scale models. Fig. 12 shows the effects of the box size on the caustics, for three of the eight extreme lens configurations. A summary of the

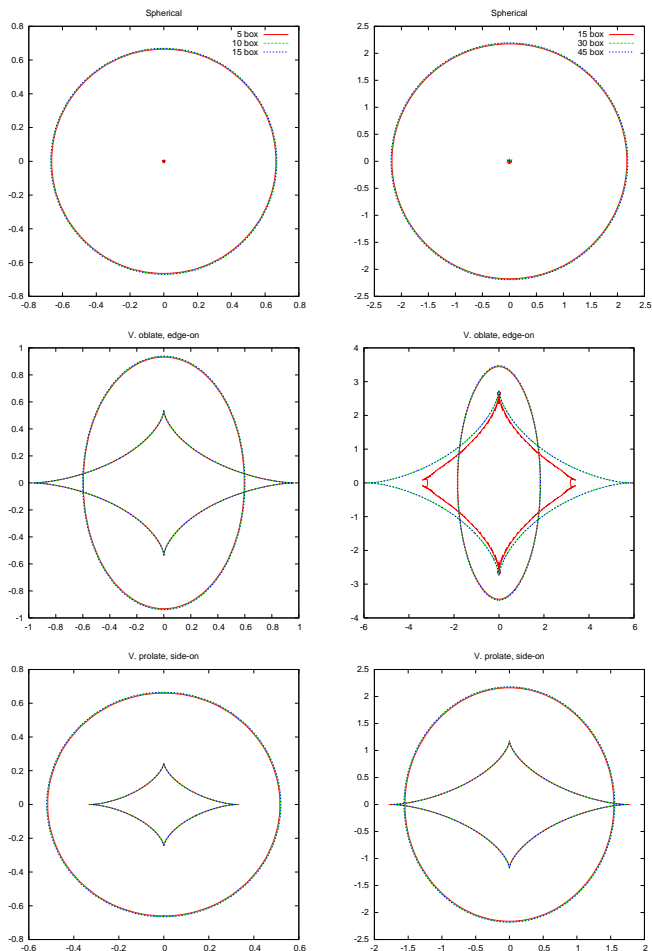


Figure 12. Source plane caustics for the lower (left) and higher (right) mass models, with the three of the eight extreme lens configurations used for the box size tests: spherical, edge-on oblate, and side-on prolate (top to bottom). Box sizes are labelled on the top plot for each mass scale. The meaning of the axes is the same as in Fig. 11.

quantitative results for all eight lens configurations are as follows:

- For the lower mass scale, the default box size of $10''$ is sufficient. There is one marginal case—the 3-image cross-section for the very oblate, edge-on model—but this cross-section is a small fraction (< 1 per cent) of the total cross-section for that model, and the statistical errors in determining it are large. The smallest ($5''$) box typically yields unbiased cross-sections that pass our 5 per cent convergence criterion, but the biased cross-sections can fail dramatically (up to 25 per cent reduction of σ_{tot} relative to the largest box), which eliminates the possibility of using such a small box.
- For the higher mass scale, the default box size of $30''$ is typically sufficient to achieve 5 per cent accuracy compared to the larger box size, though occasionally the results are marginal, particularly for highly biased cross-sections. Visually, the caustics appear to be nearly identical for the $30''$ (fiducial) and $45''$ (largest) boxes (Fig. 12), with rather bizarre and very significant distortion for the $15''$ box for

some viewing directions, for which the cross-sections are also significantly reduced.

- Some caustics appear smoother than for the corresponding cases in the resolution tests in Section 5.7. The difference comes from the fact that here we use $\gamma_{\text{dm}} = 1.5$ models, which have Einstein radii that are significantly larger than for the $\gamma_{\text{dm}} = 0.5$ models used for the resolution tests.

- The effect of insufficient box size is to shrink both the radial and tangential caustics, and to alter the shape of the tangential caustic.

The caustics and cross-sections together imply that even with the largest possible Einstein radius at each mass scale, the medium-sized boxes, $10''$ ($\simeq 43.6$ kpc) and $30''$ ($\simeq 131$ kpc), are sufficient. The box size requirement in dimensionless units is $\sim 16 R_{\text{ein}}$.

5.9 Sampling viewing angles

We are interested in the lensing properties of galaxies not only for specific viewing angles, but also when averaged over all viewing angles. We must choose how to sample the possible viewing directions in order to obtain accurate averages with as little computational effort as possible. We are guided by two principles. First, we expect the lensing quantities to vary with viewing direction in some smooth and, in the oblate and prolate cases, monotonic way. Second, this variation is more directly related to the shape of the projected surface mass density than to the viewing angles per se.

5.9.1 Sampling in projected axis ratios

Instead of directly sampling angles relative to the intrinsic axes ϑ and φ , we sample linearly in the ratios a'/a and b'/a , i.e., the projected major and minor semi-axis length a' and b' as given in equation (5), normalised by the intrinsic length scale a . Since this choice does not correspond to an equal-area sampling on the viewing sphere (i.e., uniform in $-1 \leq \cos\vartheta \leq 1$ and $0 \leq \varphi \leq 2\pi$), we need to include a weighting factor to recover accurate averages. The orientation-averaged value of some quantity f (which in our case will be a lensing cross-section) can be written as

$$\langle f \rangle = \frac{2}{\pi} \int_0^{\pi/2} \int_0^{\pi/2} f(\vartheta, \varphi) \sin\vartheta \, d\vartheta \, d\varphi, \quad (39)$$

$$= \frac{2}{\pi} \int_c^b \int_b^a f(\vartheta, \varphi) \sin\vartheta \, J(a', b') \, da' \, db', \quad (40)$$

where the expression for the Jacobian $J(a', b')$ is given in Appendix A, as is the inversion of equation (5) to find (ϑ, φ) in terms of (a', b') . In the oblate and prolate cases, one of the two integrals is irrelevant since the lensing depends on only one of the angles, but in the triaxial case both integrals are important.

By construction, the individual mass components we use have axis ratios that are constant as a function of radius. However, since the dark matter and stellar components have different intrinsic shapes (Table 2), the combined, total density has intrinsic and projected axis ratios that vary with radius (see also Fig. 9). Fortunately, the precise choice of axis ratios to use for the sampling is not terribly important, as long as it is treated properly according to equation (40).

We choose to sample in the axis ratios of the dark matter component, i.e., in what follows a'/a and b'/a always refer to the dark matter component.

There are two important issues related to the sampling:

- (i) We must first test our intuition that cross-sections vary smoothly with a'/a and b'/a . We can do this by using a large number N_s of samplings (we use $N_s = 47$ for the oblate case, $N_s = 31$ for the prolate case, and $N_s = 23 \times 15 = 345$ for the triaxial case).

- (ii) We must determine how few samplings can be used to obtain orientation-averaged cross-sections that are accurate at the 5 per cent level. We can do this by undersampling the original number of samplings and seeing how few samplings we can use while still recovering the average cross-sections to within 5 per cent.

For the viewing angle sampling tests, we use cusped density profiles with dark matter slope $\gamma_{\text{dm}} = 1.5$ and the extreme oblate and prolate shapes, since these will have the strongest variation of cross-section with inclination. We also consider the triaxial case, for which we test the sampling in both a'/a and b'/a . In addition to the total strong lensing cross-section, we require accurate recovery of the 2, 3, and 4-image cross-sections separately.

5.9.2 Variation of cross-section with projected axis ratios

We show the variation of the cross-sections with viewing angle in Fig. 13 for both mass models, using the very oblate and very prolate shapes. The symmetry of the oblate case means we only need to vary the polar viewing angle ϑ , which we accomplish by taking equal steps in a'/a . Similarly, for the prolate case we only need to vary the azimuthal viewing angle φ , again taking equal steps in a'/a . For this plots, we use our fiducial number of samplings (47 for the oblate case, and 23 for the prolate case) to generate the cross-section curves, and we show the undersampled by four case with crosses. We defer discussion of the physical intuition behind the viewing angle dependence to Paper II, and focus here on the technical issues of smoothness and sampling. It is clear that, as expected, the variation of the individual and total cross-sections is a smooth function of the projected axis ratios for prolate and oblate dark matter plus stellar density shapes.

Note that the 3-image cross-section should be identically zero for any lens configuration for which the tangential caustic lies entirely within the radial caustic. This means that σ_3 should be zero for our oblate models when b'/a is above some threshold, and for our prolate models throughout the full range of a'/a . Our numerical 3-image cross-sections are not strictly zero at a very few values of the projected axis ratio due to extremely rare errors in finding and classifying images (see Section 5.2). However, the spurious 3-image cross-sections are well below 0.1 per cent of the total cross-sections, so they are a negligible source of error.

In Fig. 14, we show the variation of the unbiased cross-sections with a'/a and b'/a for the lower mass triaxial model. (The results are very similar for the higher mass triaxial model, except for an overall difference in amplitude.) The changes for the biased cross-sections are described qualitatively. We again defer discussion of the physical intuition behind the orientation-dependence of the cross-section to Pa-

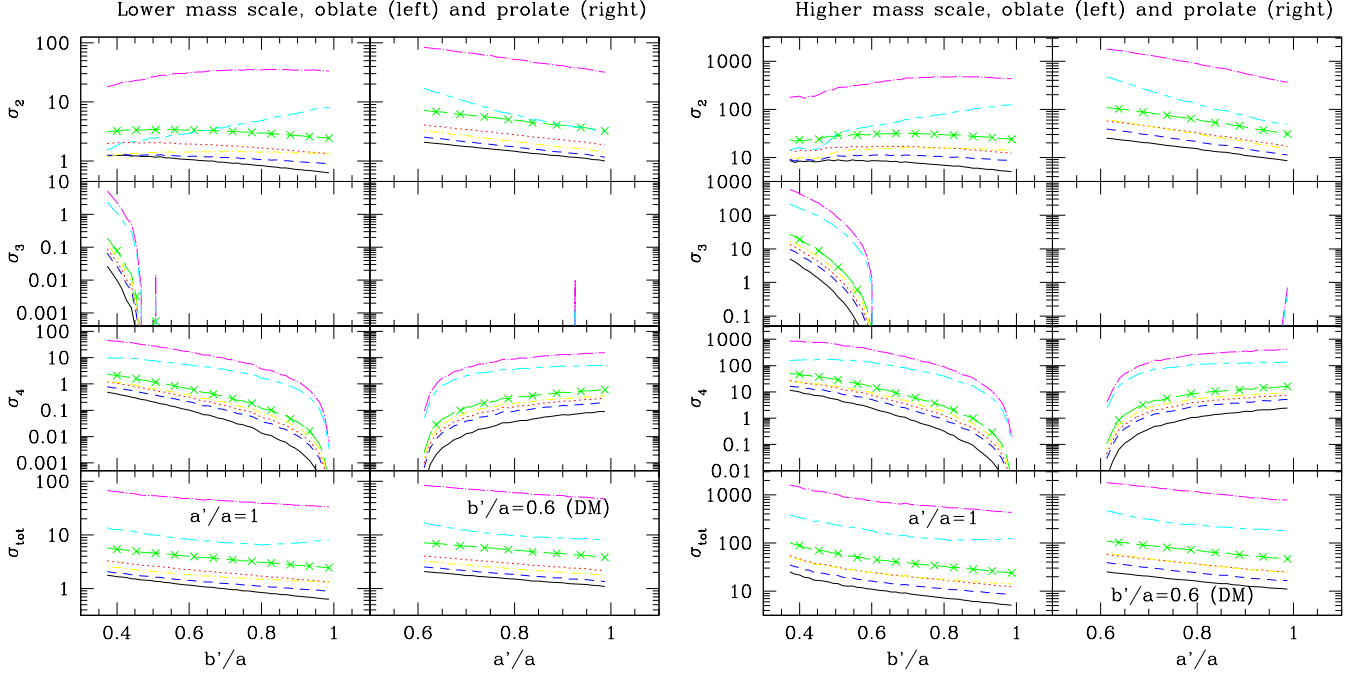


Figure 13. Lensing cross-sections for the lower (left plot) and higher (right plot) mass scale, for oblate and prolate models, for 2, 3, 4-image systems separately as labelled, and the total cross-section at the bottom. The lines are as follows: black solid = unbiased, red dotted and blue dashed = weighted by total and second-brightest magnification respectively for $0.04L_*$ limiting magnitude, green long-dashed and yellow dot-dashed = the same for $0.4L_*$ limiting magnitude, and magenta dot-long dashed and cyan short-long dashed = the same for $4L_*$ limiting magnitude. The lines show the curves resulting from our fiducial sampling in a' and b' ; crosses show our eventual choice of sampling as described in Section 5.9.3. The 3-image cross-section should be identically zero for b'/a or a'/a above some threshold; the occasional spikes at small but finite values indicate small numerical errors due to misclassification of images.

per II. Here we merely observe that for the triaxial case, the unbiased cross-sections σ_2 , σ_4 , and σ_{tot} are smooth functions of a'/a and b'/a , without multiple local minima/maxima or other features that would require dense sampling. The biased cross-sections also vary smoothly, regardless of which magnification bias mode we use. One difference is that the contours of the 2-image biased cross-section tend to lie at nearly constant a'/a , not as tilted as in the unbiased case (see Paper II).

5.9.3 Minimum number of samplings

Next we consider how few samplings we can get away with and still recover accurate results for cross-sections averaged over viewing directions. To do so, we start with our fiducial number of samplings, and compare the total average cross-sections (properly weighting each sampling using the Jacobian) when undersampling by a factor of 2, 4, and 8. In the triaxial case, we always consider undersampling by the same factor in both a'/a and b'/a . Generally, given N_s samplings in a'/a or b'/a , we have $(1 + N_s)/u$ viewing angles when undersampling by a factor of $u = 2^v$ for $v \geq 1$.

We find that for all mass scales, magnification bias modes, and numbers of images, undersampling by a factor of 4 in both a'/a and b'/a allows us to recover orientation-averaged cross-sections to within 5 per cent accuracy when compared with the full sampling. In general, 3-image systems are the most difficult to sample properly due to their strong variation with inclination (as in Fig. 13). This level

of undersampling corresponds to only 12 samplings in b'/a in the oblate case, 8 samplings in a'/a in the prolate case, and 6 (in a'/a) \times 4 (in b'/a) = 24 samplings total in the triaxial case. For reference, in Fig. 13 and 14 we indicate our chosen level of undersampling with crosses.

6 CONCLUSIONS

We have presented a flexible simulation pipeline for coherent investigations of selection and modelling biases in strong lensing surveys. We have focused on point-source lensing by two-component galaxy models meant to emulate realistic early-type, central galaxies at two different mass scales: a lower, $\sim 2L_*$ galaxy mass scale and a higher, $\sim 7L_*$ group mass scale (with L_* in the r -band). Below is a list of our main conclusions regarding the construction of the simulation pipeline for lensing by realistic galaxy models:

- We include both cusped and deprojected Sérsic density profiles, with observationally-motivated choices of masses and scale lengths, and a range in density profile parameters, separately for the stellar and dark matter component. We use seven different models for the galaxy shapes with the stellar component rounder than the dark matter component, but with the axes intrinsically aligned. [Sections 4.1–4.5]
- When we change the density profile parameters away from the adopted fiducial values, we preserve the total and virial mass of the stellar and dark matter components (respectively) by changing the density amplitude. We keep the

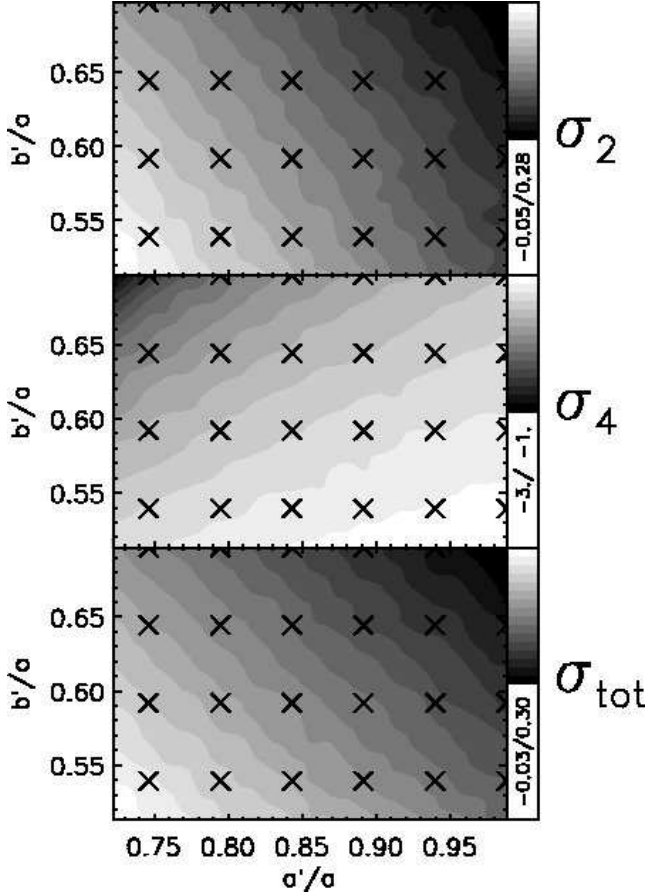


Figure 14. Base-10 logarithm of the unbiased lensing cross-sections for the lower mass, triaxial shape model, as a function of a'/a and b'/a . Note that the contour scales are different on each plot, and σ_3 is not shown because it is negligible. The crosses indicate our final choice of sampling, as described in Section 5.9.3.

scale radius fixed to comply with observed size-luminosity relations for early-type galaxies and concentration-mass relations for dark matter halos. Similarly, for the non-spherical shapes we change the scale length to preserve the mass but keep the scale radius (and hence the concentration) the same as for the fiducial spherical case. [Sections 4.3.2, 4.4.2, 4.5.2]

- We choose fiducial lens and source redshifts of 0.3 and 2.0, resulting in Einstein radii R_{ein} at about one effective radius R_e . [Section 3.2]

- We require multiple ways of handling magnification bias to sample different parts of the observed quasar luminosity function and to allow for application to different survey limitations in image resolution and flux. [Section 5.4]

- When the surface mass density is known analytically (as for our deprojected Sérsic models), we compute the corresponding lensing deflection and magnification analytically (for circular symmetry) or with numerical integrals (for elliptical symmetry). When the surface mass density cannot be computed analytically, as for the cusped models, we construct a surface density map and use Fourier methods to compute the lensing deflection and magnification. We validate and use Monte Carlo methods to calculate lensing statistics, including unbiased and biased cross-sections and image separations. [Sections 5.1–5.6]

- For our map-based lensing calculations, tests for convergence at the 5 per cent level suggest that the required map resolution is ~ 25 pixel lengths per R_{ein} , corresponding to $0.025''$ ($\simeq 0.11$ kpc) and $0.075''$ ($\simeq 0.33$ kpc) for the lower and higher mass scale, respectively. The resolution needs to be fine enough to simultaneously resolve the steepness of the inner slope of the density and recover the smoothness of the shape of the inner critical curve. Similarly, convergence tests suggest that the required box size is $\sim 16 R_{\text{ein}}$, corresponding to $10''$ ($\simeq 43.6$ kpc) and $30''$ ($\simeq 131$ kpc) for the lower and higher mass scale, respectively. [Sections 5.7 and 5.8]

- Lensing cross-sections for fairly general triaxial models vary in a smooth and monotonic way with viewing direction, which can be efficiently sampled through projected axis ratios (rather than viewing angles) of the surface density. Surprisingly few samplings are necessary: 10, 8, and 24 viewing directions can effectively determine the orientation-averaged cross-sections for oblate, prolate, and triaxial models (respectively) with 5 per cent precision. [Section 5.9]

We have implemented the construction of the realistic galaxy models and efficient computation of the corresponding surface mass density maps in IDL (see also Section 4.6). All subsequent strong lensing calculations are done with an updated and extended version of GRAVLENS. We use scripts to coordinate and analyse the extensive data flow to and from these two parts, and to make it into a coherent simulation pipeline.

Our investigations have revealed a number of useful, general points related to the interpretation of observational strong lensing results:

- In the vicinity of the Einstein radius, the intrinsic and projected logarithmic slopes of the total density are close to the values $\gamma = 2$ and $\gamma' = 1$ of an isothermal profile, for all of our galaxy models (see Figs. 3 and 5, and the text of Sec. 4.3.3). Consequently, a measurement of the total density profile near the Einstein radius cannot (alone) be used to determine the dark matter inner slope for a two-component model. This is a non-trivial conclusion given the variety of intrinsic non-isothermal density profiles used for both the stellar and dark matter component, including profiles with a true central cusp and those that do not asymptote to a particular inner slope at any scale.

- We also find that the lensing deflection curves are nearly flat around (and even beyond) R_{ein} , similar to a flat deflection curve for an isothermal model (see Fig. 7), particularly for the lower-mass galaxy scale. This again implies that constraints from strong lensing cannot be extrapolated to radii much smaller or larger than the Einstein radius. We emphasize that the parameters for the galaxy models were *not* a priori chosen to mimic this effect, but that it truly seems to be an “isothermal conspiracy” (e.g., Rusin et al. 2003).

- Because of our assumption of alignment between the intrinsic axes of the stellar and dark matter components, only the two shape models with a triaxial dark matter component and a rounder (triaxial or oblate) stellar component can have a significant misalignment between their projected axes. Even then, significant misalignment occurs only for a limited number of viewing directions, several of which lead to a relatively round projected stellar component such that the misalignment is not very important in practice (the position angle of a round stellar component is on the sky, after all,

difficult to establish). The small misalignments inferred for relatively isolated lens systems, as well as detailed dynamical modelling of early-type galaxies, support near intrinsic alignment between stars and dark matter (see Section 4.4.3).

In Paper II, we use the flexibility of the pipeline to study selection biases related to the galaxy mass, shape, orientation, and various parameters of the dark matter and stellar profiles. In subsequent work, we will investigate modelling biases by analysing the mock lens systems produced by the pipeline using the lens modelling tools within the GRAVLENS package. We have therefore created a lensing simulation pipeline that will be crucial for deriving inferences about galaxy density profiles and shapes, H_0 , and other parameters from the thousands of lenses that will be discovered in the coming years in large photometric surveys such as Pan-STARRS, LSST, SNAP, and SKA.

Furthermore, following a similar approach as in van de Ven et al. (2008a), we plan to extend the pipeline to produce projected kinematics of our galaxy models that mimic the two-dimensional kinematic observations of early-type galaxies. We will then investigate how well we can expect to recover the intrinsic density profile and shape of early-type galaxies, based solely on dynamical models fitted to these simulated kinematics, or on a combination of kinematics and strong lensing (using techniques similar to van de Ven et al. 2008b). This work will be valuable for understanding the modelling biases in analyses of the kinematic data that are becoming available for hundreds of galaxies at increasing redshifts, and for understanding both modelling and selection biases in joint lensing+kinematics studies.

ACKNOWLEDGMENTS

We are thankful to Chung-Pei Ma, Michael Kuhlen and Scott Tremaine for stimulating discussions on related topics. We thank the referees for constructive comments and suggestions. This work has made use of the public CONTRA software package provided by Oleg Gnedin to perform adiabatic contraction calculations.

GvdV and RM acknowledge support provided by NASA through Hubble Fellowship grants HST-HF-01202.01-A and HST-HF-01199.02-A, respectively, awarded by the Space Telescope Science Institute, which is operated by the Association of Universities for Research in Astronomy, Inc., for NASA, under contract NAS 5-26555. CRK acknowledges support from NSF through grant AST-0747311, and from NASA through grant HST-AR-11270.01-A from the Space Telescope Science Institute, which is operated by the Association of Universities for Research in Astronomy, Inc., under NASA contract NAS 5-26555.

REFERENCES

- Allen S. W., Etori S., Fabian A. C., 2001, *MNRAS*, 324, 877
 Allen S. W., Schmidt R. W., Fabian A. C., 2002, *MNRAS*, 335, 256
 Allgood B., Flores R. A., Primack J. R., Kravtsov A. V., Wechsler R. H., Faltenbacher A., Bullock J. S., 2006, *MNRAS*, 367, 1781
 Baltz E. A., Marshall P., Oguri M., 2009, *JCAP*, 1, 15
 Bartelmann M., Schneider P., 2001, *Phys. Rep.*, 340, 291
 Bernardi M., Hyde J. B., Sheth R. K., Miller C. J., Nichol R. C., 2007, *AJ*, 133, 1741
 Blandford R., Narayan R., 1986, *ApJ*, 310, 568
 Blanton M. R., et al., 2003, *ApJ*, 592, 819
 Blumenthal G. R., Faber S. M., Flores R., Primack J. R., 1986, *ApJ*, 301, 27
 Bolton A. S., Burles S., Koopmans L. V. E., Treu T., Gavazzi R., Moustakas L. A., Wayth R., Schlegel D. J., 2008a, *ApJ*, 682, 964
 Bolton A. S., Burles S., Koopmans L. V. E., Treu T., Moustakas L. A., 2006, *ApJ*, 638, 703
 Bolton A. S., Burles S., Schlegel D. J., Eisenstein D. J., Brinkmann J., 2004, *AJ*, 127, 1860
 Bolton A. S., Treu T., Koopmans L. V. E., Gavazzi R., Moustakas L. A., Burles S., Schlegel D. J., Wayth R., 2008b, *ApJ*, 684, 248
 Bosma A., 1981, *AJ*, 86, 1825
 Bouché N., et al., 2007, *ApJ*, 671, 303
 Bullock J. S., Kolatt T. S., Sigad Y., Somerville R. S., Kravtsov A. V., Klypin A. A., Primack J. R., Dekel A., 2001, *MNRAS*, 321, 559
 Burke W. L., 1981, *ApJ*, 244, L1
 Cappellari M., et al., 2006, *MNRAS*, 366, 1126
 —, 2007, *MNRAS*, 379, 418
 Cardone V. F., 2004, *A&A*, 415, 839
 Ciotti L., Bertin G., 1999, *A&A*, 352, 447
 Cohn J. D., Kochanek C. S., McLeod B. A., Keeton C. R., 2001, *ApJ*, 554, 1216
 Côté P., McLaughlin D. E., Cohen J. G., Blakeslee J. P., 2003, *ApJ*, 591, 850
 Croom S. M., Smith R. J., Boyle B. J., Shanks T., Miller L., Outram P. J., Loaring N. S., 2004, *MNRAS*, 349, 1397
 de Zeeuw T., Franx M., 1989, *ApJ*, 343, 617
 di Serego Alighieri S., et al., 2005, *A&A*, 442, 125
 Dobler G., Keeton C. R., Bolton A. S., Burles S., 2008, *ApJ*, 685, 57
 Douglas N. G., et al., 2007, *ApJ*, 664, 257
 Einasto J., 1965, *Trudy Inst. Astrofiz. Alma-Ata*, 5, 87
 Emsellem E., et al., 2004, *MNRAS*, 352, 721
 —, 2007, *MNRAS*, 379, 401
 Emsellem E., Monnet G., Bacon R., 1994, *A&A*, 285, 723
 Faber S. M., et al., 2007, *ApJ*, 665, 265
 Fassnacht C. D., Marshall P. J., Baltz A. E., Blandford R. D., Schechter P. L., Tyson J. A., 2004, in *Bulletin of the American Astronomical Society*, Vol. 36, p. 1531
 Ferrarese L., et al., 2006, *ApJS*, 164, 334
 Ferreras I., Saha P., Williams L. L. R., 2005, *ApJ*, 623, L5
 Finch T. K., Carlivati L. P., Winn J. N., Schechter P. L., 2002, *ApJ*, 577, 51
 Franx M., 1988, *MNRAS*, 231, 285
 Franx M., van Gorkom J. H., de Zeeuw T., 1994, *ApJ*, 436, 642
 Fukugita M., Shimasaku K., Ichikawa T., 1995, *PASP*, 107, 945
 Fukugita M., Turner E. L., 1991, *MNRAS*, 253, 99
 Gao, L. and Navarro, J. F. and Cole, S. and Frenk, C. S.

- and White, S. D. M. and Springel, V. and Jenkins, A. and Neto, A. F., 2008, *MNRAS*, 387, 536
- Gavazzi R., Treu T., Rhodes J. D., Koopmans L. V. E., Bolton A. S., Burles S., Massey R. J., Moustakas L. A., 2007, *ApJ*, 667, 176
- Gnedin O. Y., Kravtsov A. V., Klypin A. A., Nagai D., 2004, *ApJ*, 616, 16
- Hernquist L., 1990, *ApJ*, 356, 359
- Hogg D. W., 1999, preprint (astro-ph/9905116)
- Huterer D., Keeton C. R., Ma C.-P., 2005, *ApJ*, 624, 34
- Inada N., et al., 2003, *Nature*, 426, 810
- Jaffe W., 1983, *MNRAS*, 202, 995
- Jiang G., Kochanek C. S., 2007, *ApJ*, 671, 1568
- Jiang L., et al., 2006, *AJ*, 131, 2788
- Jing Y. P., Suto Y., 2002, *ApJ*, 574, 538
- Kaiser N., 2004, in *SPIE Conference*, Vol. 5489, *Ground-based Telescopes*, ed. Oschmann, Jr., J. M., pp. 11–22
- Kauffmann G., et al., 2003, *MNRAS*, 341, 33
- Kazantzidis S., Kravtsov A. V., Zentner A. R., Allgood B., Nagai D., Moore B., 2004, *ApJ*, 611, L73
- Keeton C. R., 2001a, preprint (astro-ph/0102341)
- , 2001b, preprint (astro-ph/0102340)
- Keeton C. R., Kochanek C. S., Falco E. E., 1998, *ApJ*, 509, 561
- Keeton C. R., Zabludoff A. I., 2004, *ApJ*, 612, 660
- Kneib J.-P., Hudelot P., Ellis R. S., Treu T., Smith G. P., Marshall P., Czoske O., Smail I., Natarajan P., 2003, *ApJ*, 598, 804
- Kochanek C. S., 2002a, in *The Shapes of Galaxies and their Dark Halos*, ed. Natarajan, P., p. 62
- , 2002b, *ApJ*, 578, 25
- , 2006, in *Saas-Fee Advanced Course 33: Gravitational Lensing: Strong, Weak and Micro*, Meylan G., Jetzer P., North P., Schneider P., Kochanek C. S., Wambsganss J., eds., pp. 91–268
- Koopmans L. V. E., Browne I. W. A., Jackson N. J., 2004, *New Astronomy Review*, 48, 1085
- Koopmans L. V. E., Treu T., Bolton A. S., Burles S., Moustakas L. A., 2006, *ApJ*, 649, 599
- Kormendy J., 1977, *ApJ*, 218, 333
- Kuhlen M., Keeton C. R., Madau P., 2004, *ApJ*, 601, 104
- La Barbera F., Busarello G., Merluzzi P., Massarotti M., Capaccioli M., 2003, *ApJ*, 595, 127
- Lambas D. G., Maddox S. J., Loveday J., 1992, *MNRAS*, 258, 404
- Limousin M., Richard J., Jullo E., Kneib J.-P., Fort B., Soucaill G., Elíasdóttir Á., Natarajan P., Ellis R. S., Smail I., Czoske O., Smith G. P., Hudelot P., Bardeau S., Ebeling H., Egami E., Knudsen K. K., 2007, *ApJ*, 668, 643
- Mandelbaum R., Seljak U., Cool R. J., Blanton M., Hirata C. M., Brinkmann J., 2006a, *MNRAS*, 372, 758
- Mandelbaum R., Seljak U., Kauffmann G., Hirata C. M., Brinkmann J., 2006b, *MNRAS*, 368, 715
- Mandelbaum R., van de Ven G., Keeton C. R., 2008, *MNRAS*, submitted [Paper II]
- Marshall P., Blandford R., Sako M., 2005, *New Astronomy Review*, 49, 387
- McDermid R. M., et al., 2006, *MNRAS*, 373, 906
- Merritt D., Graham A. W., Moore B., Diemand J., Terzić B., 2006, *AJ*, 132, 2685
- Merritt D., Navarro J. F., Ludlow A., Jenkins A., 2005, *ApJ*, 624, L85
- Mitchell J. L., Keeton C. R., Frieman J. A., Sheth R. K., 2005, *ApJ*, 622, 81
- Momcheva I., Williams K., Keeton C., Zabludoff A., 2006, *ApJ*, 641, 169
- Morganti R., et al., 2006, *MNRAS*, 371, 157
- Morganti R., Sadler E. M., Oosterloo T., Pizzella A., Bertola F., 1997, *AJ*, 113, 937
- Naab T., Johansson P. H., Ostriker J. P., Efstathiou G., 2007, *ApJ*, 658, 710
- Navarro J. F., et al., 2004, *MNRAS*, 349, 1039
- Navarro J. F., Frenk C. S., White S. D. M., 1997, *ApJ*, 490, 493
- Noordermeer E., van der Hulst J. M., Sancisi R., Swaters R. S., van Albada T. S., 2007, *MNRAS*, 376, 1513
- Oguri M., 2007, *ApJ*, 660, 1
- Oguri M., Keeton C. R., 2004, *ApJ*, 610, 663
- Persic M., Salucci P., Stel F., 1996, *MNRAS*, 281, 27
- Prugniel P., Simien F., 1997, *A&A*, 321, 111
- Read J. I., Trentham N., 2005, *Royal Society of London Philosophical Transactions Series A*, 363, 2693
- Richards G. T., et al., 2006, *AJ*, 131, 2766
- Rudd D. H., Zentner A. R., Kravtsov A. V., 2008, *ApJ*, 672, 19
- Rusin D., et al., 2003, *ApJ*, 587, 143
- Rusin D., Kochanek C. S., 2005, *ApJ*, 623, 666
- Rusin D., Kochanek C. S., Keeton C. R., 2003, *ApJ*, 595, 29
- Rybicki G. B., 1987, in *IAU Symp. 127: Structure and Dynamics of Elliptical Galaxies*, ed. P. T. de Zeeuw, p. 397
- Salvador-Solé E., Manrique A., González-Casado G., Hansen S. H., 2007, *ApJ*, 666, 181
- Schneider P., Ehlers J., Falco E. E., 1992, *Gravitational Lenses*. Springer-Verlag Berlin Heidelberg New York. Also *Astronomy and Astrophysics Library*
- Schramm T., 1990, *A&A*, 231, 19
- Sellwood J. A., McGaugh S. S., 2005, *ApJ*, 634, 70
- Sérsic J. L., 1968, *Atlas de galaxias australes*. Cordoba, Argentina: Observatorio Astronomico, 1968
- Shen S., Mo H. J., White S. D. M., Blanton M. R., Kauffmann G., Voges W., Brinkmann J., Csabai I., 2003, *MNRAS*, 343, 978
- Treu T., Koopmans L. V. E., 2004, *ApJ*, 611, 739
- Turner E. L., Ostriker J. P., Gott III J. R., 1984, *ApJ*, 284, 1
- Tyson J. A., 2002, in *SPIE Conference*, Vol. 4836, *Survey and Other Telescope Technologies and Discoveries*, eds Tyson, J. Anthony; Wolff, Sidney, pp. 10–20
- van Albada T. S., Bahcall J. N., Begeman K., Sancisi R., 1985, *ApJ*, 295, 305
- van de Ven G., de Zeeuw P. T., van den Bosch R. C. E., 2008a, *MNRAS*, 385, 614
- van de Ven G., Falcón-Barroso J., McDermid R. M., Cappellari M., Miller B. W., de Zeeuw P. T., 2008b, preprint (arXiv:0807.4175)
- van den Bosch R. C. E., 2008, PhD thesis, Leiden Observatory, Leiden University, P.O. Box 9513, 2300 RA Leiden, The Netherlands
- van den Bosch R. C. E., van de Ven G., Verolme E. K., Cappellari M., de Zeeuw P. T., 2008, *MNRAS*, 385, 647
- van der Marel R. P., van Dokkum P. G., 2007, *ApJ*, 668, 738
- Vikhlinin A., Kravtsov A., Forman W., Jones C., Marke-

- vitch M., Murray S. S., Van Speybroeck L., 2006, ApJ, 640, 691
- Vikhlinin A., Markevitch M., Murray S. S., Jones C., Forman W., Van Speybroeck L., 2005, ApJ, 628, 655
- Wechsler R. H., Bullock J. S., Primack J. R., Kravtsov A. V., Dekel A., 2002, ApJ, 568, 52
- Weijmans A.-M., Krajnović D., van de Ven G., Oosterloo T. A., Morganti R., de Zeeuw P. T., 2008, MNRAS, 383, 1343
- Williams K. A., Momcheva I., Keeton C. R., Zabludoff A. I., Lehár J., 2006, ApJ, 646, 85
- Winn J. N., Rusin D., Kochanek C. S., 2004, Nature, 427, 613
- Young P., 1980, ApJ, 242, 1232

APPENDIX A: SAMPLING OF VIEWING DIRECTION VIA PROJECTED AXIS RATIOS

The smooth variation in lensing cross-section with viewing direction is more directly related to the (elliptic) shape of the surface mass density than the viewing angles. Hence, instead of sampling directly ϑ and φ , we sample linearly in the projected axis ratios a' and b' given in equation (5). Inversion of the latter relation yields

$$\cos^2 \vartheta = \frac{(a'^2 - c^2)(b'^2 - c^2)}{(a^2 - c^2)(b^2 - c^2)}, \quad (\text{A1})$$

$$\tan^2 \varphi = \frac{(a'^2 - b^2)(b^2 - b'^2)(a^2 - c^2)}{(a^2 - a'^2)(a^2 - b'^2)(b^2 - c^2)}. \quad (\text{A2})$$

The Jacobian $J(a', b')$ of the transformation between (ϑ, φ) and (a', b') is given by

$$\sin \vartheta J(a', b') = \frac{a' b' (a'^2 - b'^2)(b^2 - c^2)}{(a'^2 - b^2)(b^2 - b'^2)(a'^2 - c^2)(b^2 - c^2)}. \quad (\text{A3})$$

In the axisymmetric limit one of the viewing angles becomes redundant. In the oblate case ($a = b > c$), we set, without loss of generality, $\varphi = \pi/2$ so that $a' = a$, and

$$\cos^2 \vartheta = \frac{b'^2 - c^2}{a^2 - c^2}, \quad \sin \vartheta d\vartheta = \frac{b' db'}{\sqrt{(a^2 - c^2)(b'^2 - c^2)}}. \quad (\text{A4})$$

Similarly, in the prolate case ($a > b = c$) we take $\vartheta = \pi/2$ so that $b' = c$, and

$$\tan^2 \varphi = \frac{a'^2 - c^2}{a^2 - a'^2}, \quad d\varphi = \frac{a' da'}{\sqrt{(a^2 - a'^2)(a'^2 - c^2)}}. \quad (\text{A5})$$

